Theory of Incoherent-Light Temporal Imaging Systems Based on a Temporal Pinhole

Bo Li and José Azaña, *Member, IEEE*

***Abstract*—We present a comprehensive consistent theoretical analysis of a set of recently demonstrated schemes for temporal imaging of incoherent-light intensity waveforms based on the time-domain pinhole concept. Schemes analyzed here include temporal magnification and compression systems, time-to-frequency mapping, and frequency-to-time mapping processes, all involving a suitable combination of optical dispersive lines and a short temporal gate (time-domain pinhole). This paper reports formal derivations of the main performance specifications in the studied incoherent-light schemes, including mapping factors and precise estimates of time/frequency resolutions and operation windows (temporal/spectral field of view), as a function of design parameters, namely dispersion values and pinhole duration. Design equations for system performance optimization are also obtained and theoretical assumptions and design tradeoffs are pointed out and discussed. Our theoretical findings are in agreement with previous simulation and experimental results and are further validated in this report.**

***Index Terms*—Frequency-to-time mapping, incoherent-light signal processing, temporal imaging, temporal pinhole, time-to-frequency mapping.**

I. Introduction

THERE is a mathematical equivalence between free-space diffraction of a spatial field and chromatic dispersion of a temporal waveform, which is referred to as space-time duality [1]–[6]. Based on this space-time duality, the concept of a "time lens" has been proposed and extensively used. A time lens is the temporal equivalent of a spatial thin lens and it can be practically implemented by imparting a quadratic temporal phase shift across the waveform under analysis. Using the mature concepts of free-space Fourier optics, a wide range of operations have been realized on time-domain signals using a suitable combination of dispersion lines and time lenses.

Functionalities enabled by the space-time duality include temporal imaging [2]–[20] and other related concepts, more prominently, time-to-frequency mapping [3], [5], [7], [13]–[15], [17], [19], [21] and frequency-to-time mapping, also referred to as real-time Fourier transformation [3], [5], [7], [13]–[15], [17], [19], [22], [23]. Temporal imaging involves magnification or compression of the temporal axis of an incoming waveform without distorting the waveform shape along the time domain. Time-to-frequency (frequency-to-time) mapping refers to a process by which the input temporal waveform (spectrum) is transferred into the output spectrum (temporal waveform). These operations provide novel, unique methods for generation [1], [5], [14], [17], [23], [24], measurement [2], [3], [6], [10], [12], [16], [21], [22], cloaking [18], [20] and processing [4], [7]–[9], [11], [13], [15], [18]–[20] of time-domain waveforms, particularly electronic and radio-frequency (RF) signals [7], [11], [13]–[15], [19], and ultrafast optical information [1]–[6], [10], [12], [14], [16]–[23]. Conventional temporal imaging and related systems have been implemented by coherent optics [1]–[23]. In particular, highly-performing temporal imaging systems such as those based on four-wave mixing [6], [16]–[18], [21] and time-stretch systems [7], [11], [13]–[15], [19] typically require the use of ultrashort pulse laser sources. Generally speaking, performance improvements in these temporal imaging platforms, e.g., evaluated in the form of time-bandwidth product, require the use of larger pulse frequency (wavelength) bandwidths, which poses practical implementation challenges. In contrast, broadband incoherent light sources can be produced in a much more practical and simpler fashion than their coherent counterparts: temporally incoherent light is intrinsically broadband while complex and costly techniques (e.g., mode locking) are needed to achieve phase locking of the entire spectral content of a broadband light source. Based on this important practical advantage, mechanisms have been demonstrated in the recent past for temporal dispersion of incoherent-light intensity waveforms [25]–[31], including frequency-to-time mapping operations. More recently, we have proposed and experimentally demonstrated the first scheme for temporal imaging of incoherent-light intensity waveforms [32]. The demonstrated system can be designed to implement both temporal magnification and compression of the intensity waveform under analysis and it also inherently implements time-to-frequency mapping of the waveform. Different to the recently proposed incoherent-light time-stretch scheme [33], [34], the scheme is based on a temporal pinhole camera, namely the time-domain equivalent of a classical pinhole camera illuminated by a totally incoherent light source [4], [32].

In this work, we report a comprehensive theoretical analysis of incoherent-light temporal imaging and time-to-frequency mapping of intensity waveforms using the concept of a temporal pinhole camera. We provide a detailed derivation of the temporal impulse response functions of the corresponding schemes; the resulting equations provide analytical estimates of the main performance specifications and trade-offs of the analyzed systems, particularly magnification or time-to-frequency scaling factors, and temporal/frequency resolutions versus operation time

Manuscript received December 5, 2015; revised February 19, 2016; accepted March 18, 2016. Date of publication March 28, 2016; date of current version April 30, 2016. This work was supported in part by the Natural Science and Engineering research Council of Canada and the China Scholarship Council for graduate fellowships.

The authors are with the Institut National de la Recherche Scientifique, Energie, Matériaux et Télécommunications, Montréal, QC H5A 1K6, Canada (e-mail: liboresearch@gmail.com; azana@emt.inrs.ca).

Color versions of one or more of the figures in this paper are available online at http://ieeexplore.ieee.org.

Digital Object Identifier 10.1109/JLT.2016.2547915

window (temporal field of view), as a function of the system design specifications, e.g., light source bandwidth, dispersion values, temporal pinhole shape and duration. The derived estimates are validated through numerical and experimental results.

More generally, the conducted analysis shows a useful, intuitive methodology for analysis of photonic signal processing systems based on incoherent light waves. Indeed, in this work, we also apply this same methodology to the study of a closely related process, namely frequency-to-time mapping of incoherent-light intensity waveforms using a short temporal gate followed by dispersion [25], [27], [28], [30]. Incoherent-light frequency-to-time mapping has been previously described using general coherence theory arguments. In this work, we provide an alternative interpretation of this same technique, consistently with the rest of the incoherent-light temporal imaging processes described here. In particular, our description considers the short temporal gate as a temporal pinhole. In line with the other studied systems, such an interpretation allows us to provide precise estimates of the optimal temporal pinhole duration and the resulting performance specifications.

The temporal pinhole camera concept was first proposed and theoretically analyzed by Kolner [4]. This previous work is the springboard of the study reported here, which advances the analysis in several important directions, particularly (i) by focusing and developing further the problem of incoherent light and (ii) by coming out with a formalism that provides a single, general framework for analysis of three different incoherent-light-based operations using the pinhole concept, namely temporal imaging, time-to-frequency mapping and frequency-to-time mapping.

II. Principle of Operation

The proposed scheme for incoherent-light temporal imaging is illustrated in Fig. 1(b). The proposed method is a time-domain equivalent of a classical pinhole camera illuminated by a totally incoherent light source, as shown in Fig. 1(a). The time-domain scheme is essentially an incoherent-light implementation of the temporal pinhole camera [5], [40].

In relation to the diagram in Fig. 1(b), light from a broadband (temporally) incoherent light source is intensity-modulated by the input RF waveform to be processed. The intensity-modulated light is dispersed through the input dispersion, which provides a group-delay dispersion of $\ddot{\Phi}_{\mathrm{In}}$ (slope of group delay as a function of radial frequency) over the entire bandwidth of the light source. The dispersed light is then sent through the temporal pinhole, which is implemented by a second temporal intensity modulation process with a short pulse waveform. Finally, the resulting light is dispersed by the output dispersion, providing a linear group-delay with slope $\ddot{\Phi}_{\mathrm{Out}}$. The averaged optical intensity profile at the output of the system is a temporally scaled (magnified or compressed) image of the input intensity waveform. No strict imaging condition needs to be satisfied to achieve the desired temporal imaging process, in contrast to a conventional time-lens-based system [1]–[6].

As discussed previously [32], the described temporal imaging process can be described as being composed of two main steps, which are time-to-frequency mapping of the input intensity waveform, implemented at the output of the temporal pinhole modulation process, and frequency-to-time mapping subsequently induced by the output dispersion. These steps are illustrated in Fig. 1(c) through a representation of the evolution of a temporal impulse along the system. The input dispersion maps the light source spectrum along the time domain, inducing an averaged linear frequency chirp of slope $1/\ddot{\Phi}_{\mathrm{In}}$ along the duration of the dispersed waveform. Because the temporal pinhole temporally filters the chirped light within a short time width at

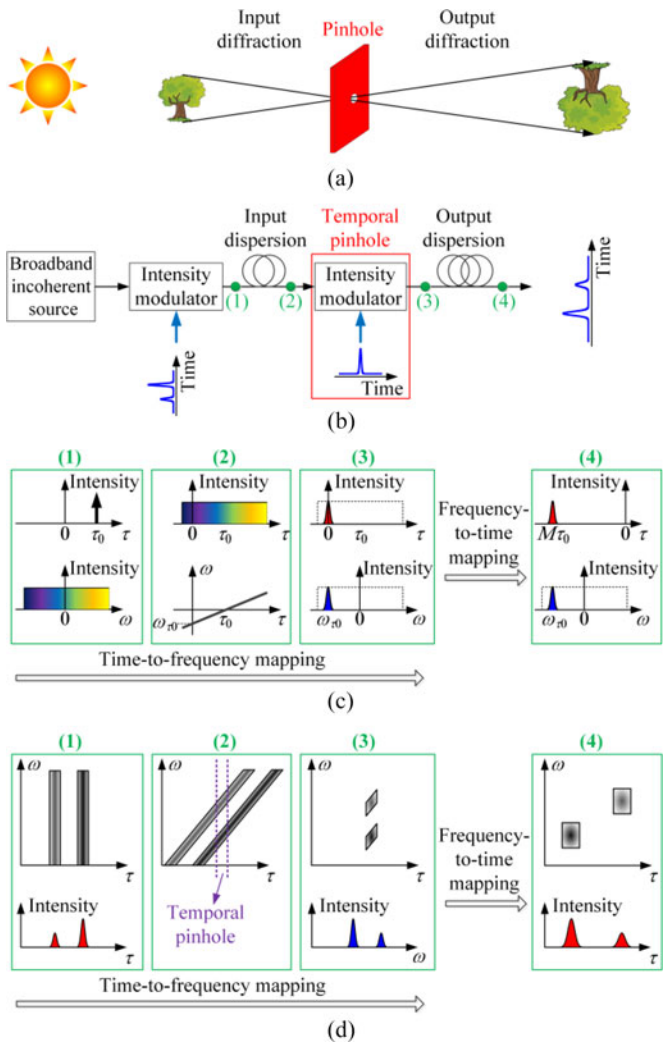

Fig. 1. Incoherent-light temporal imaging concept. (a) Illustration of an incoherent-light spatial imaging system, i.e. pinhole camera, based on free-space diffraction and a pinhole. (b) Illustration of an incoherent-light temporal imaging system, which is established as the time-domain equivalent of the incoherent-light spatial imaging system. Temporal group-delay dispersion and intensity modulation with a fast temporal shutter (temporal pinhole) are employed in this system. (c) Illustration of the impulse response of the temporal imaging system in (b). For a linear system, the system output is the impulse response when the input is a temporal impulse. The profile of the signal is converted to frequency domain through time-to-frequency mapping during the first stage of the system. Frequency-to-time mapping is then performed by propagation through the output dispersion. (d) Evolution of a two-pulse signal during the temporal imaging process. Top plots illustrate the time-frequency energy distribution of the signal whereas the bottom plots show the signals' temporal waveform or energy spectrum at the corresponding stage. All represented waveforms, spectra, and the instantaneous frequency curve, are averaged profiles.

a reference time, a corresponding narrow portion of spectrum is selected. The selected spectrum is centered at the frequency of $\omega_{\tau 0}$, which is dependent on the dispersion amount and the location of τ_0, i.e., $\omega_{\tau 0} = -\tau_0/\ddot{\Phi}_{\rm In}$, performing the predicted time-to-frequency mapping. As the temporal pinhole is a short time gate, frequency-to-time mapping is subsequently realized by the output dispersion [25], [27], with a scaling factor of $\ddot{\Phi}_{\rm Out}$. Consequently, the system response to the input impulse is a short pulse located at $M\tau_0$, where $M = -\ddot{\Phi}_{\rm Out}/\ddot{\Phi}_{\rm In}$ defines then the *temporal magnification factor* of the imaging system. To fully demonstrate how does a complex waveform transform, Fig. 1(d) shows the evolution a two-pulse signal during the temporal imaging process.

A preliminary assumption of our theoretical analysis is that the used light source is totally incoherent, so-called a white-noise light source. Strictly, this assumption implies that the coherence time of the source tends to zero and that the corresponding source spectrum is uniform over an infinite bandwidth. This assumption allows simplifying the analysis while still providing precise estimates of the parameters of interest. It is known that the temporal impulse response function of a linear system illuminated by totally incoherent light source can be obtained by squaring the magnitude of the field impulse response of the corresponding coherent system [35], [36]. When the input light is completely incoherent, the intensity of the light at each point in the output is a weighted superposition of contributions from intensities at all points of the input, i.e., interference does not occur and the intensities simply add [35]. Based on this principle, we will derive the impulse response functions of the incoherent-light temporal imaging processes under analysis. Conditions to be satisfied by a practical light source will be also given to ensure that the provided descriptions and obtained results are still valid.

The following Section II-A reports our theoretical analysis of incoherent-light time-to-frequency mapping using a temporal pinhole; Section II-B is devoted to the theory of the related system for incoherent-light temporal imaging; finally, Section II-C presents an alternative description of the process of frequency-to-time mapping of incoherent light within the framework of the temporal pinhole theory.

A. Incoherent-Light Time-to-Frequency Mapping

Time-to-frequency mapping of the input intensity waveform is implemented by a system involving an input dispersion line and a following temporal-pinhole modulation process. In our analysis, the light source is first assumed to be totally incoherent. As such, the temporal impulse response function of the system is obtained by squaring the magnitude of the field impulse response of the corresponding coherent system. The Fourier transform definition used in the text is

$$\mathrm{G}(\tau) = \mathscr{F}^{-1}\left[\tilde{G}(\omega)\right] = \frac{1}{\sqrt{2\pi}}\int_{-\infty}^{\infty}\tilde{G}(\omega)\, e^{j\omega\tau}\, d\omega, \quad (1)$$

$$\tilde{G}(\omega) = \mathscr{F}\left[\mathrm{G}(\tau)\right] = \frac{1}{\sqrt{2\pi}}\int_{-\infty}^{\infty}\mathrm{G}(\tau)\, e^{-j\omega\tau}\, d\tau, \quad (2)$$

where $\mathscr{F}$ and $\mathscr{F}^{-1}$ refer to Fourier transformation and inverse Fourier transformation, respectively.

As shown in Fig. 1(b), the input optical waveform, generated by modulating the input optical light, is represented as an impulse at τ_0, which is given by

$$A_{\rm In}(\tau, \tau_0) = \delta(\tau - \tau_0). \quad (3)$$

The complex temporal envelope of the light after input dispersion is

$$A_{\rm ID}(\tau, \tau_0) = A_{\rm In}(\tau, \tau_0) \otimes h_{\rm ID}(\tau) = h_{\rm ID}(\tau - \tau_0), \quad (4)$$

where $\otimes$ represents convolution, $h_{\rm ID}(\tau) = h_{0,\rm ID}\exp[(j\tau^2)/(2\ddot{\Phi}_{\rm ID})]$ is the complex envelope of the impulse response function of the input dispersion, $\ddot{\Phi}_{\rm ID}$ is the group-delay dispersion, defined as the slope of the group delay curve as function of radial frequency, and $h_{0,\rm ID} = 1/\sqrt{j2\pi\ddot{\Phi}_{\rm ID}}$ [3], [22]. Notice that in our derivations, τ is normalized time so that the average group-delay in each of the constituting elements is ignored in the analysis [3].

The dispersed light is subsequently modulated by the temporal pinhole. Following propagation through the temporal pinhole, the spectral amplitude of the modulated light is given by

$$\begin{aligned}
\tilde{A}_P(\omega, \tau_0) &= \mathscr{F}\left[A_P(\tau, \tau_0)\right] = \mathscr{F}\left[A_{\rm ID}(\tau, \tau_0)\, P(\tau)\right] \\
&= \frac{1}{\sqrt{2\pi}}\int_{-\infty}^{\infty} h_{0,\rm ID}\exp\frac{j(\tau-\tau_0)^2}{2\ddot{\Phi}_{\rm ID}}\, P(\tau)\exp(-j\omega\tau)\, d\tau \\
&\xrightarrow{\omega_T = -\ddot{\Phi}_{ID}\omega} \frac{1}{\sqrt{2\pi}}\exp\left[\frac{-j}{2\ddot{\Phi}_{\rm ID}}\left(\omega_T^2 - 2\tau_0\omega_T\right)\right]\int_{-\infty}^{\infty} P(\tau) \\
&\quad \times h_{0,\rm ID}\exp\left\{\frac{j}{2\ddot{\Phi}_{\rm ID}}\left[(\tau_0 - \omega_T) - \tau\right]^2\right\} d\tau \\
&= \frac{1}{\sqrt{2\pi}}\exp\left[\frac{-j}{2\ddot{\Phi}_{\rm ID}}\left(\omega_T^2 - 2\tau_0\omega_T\right)\right] \\
&\quad \times P(\tau_0 - \omega_T) \otimes h_{\rm ID}(\tau_0 - \omega_T), \quad (5)
\end{aligned}$$

in which $A_P(\tau, \tau_0)$ is the signal's complex temporal amplitude at the temporal pinhole output, ω is the base-band frequency variable around the central optical frequency of interest, and $\omega_T = -\ddot{\Phi}_{\rm ID}\omega$.

As shown by Eq. (5), apart from the quadratic phase preceding the convolution, $\tilde{A}_P(\omega, \tau_0)$, the spectrum of the impulse response immediately after the pinhole for a temporal impulse at τ_0, depends only on the difference in $\tau_0 - \omega_T$. Assuming a coherent input optical waveform, with a temporal amplitude given by $A_{\rm In}(\tau)$, the spectral amplitude of the output signal can be calculated as follows:

$$\tilde{A}_{\rm Out}(\omega) = \int_{-\infty}^{\infty}\tilde{A}_P(\omega, \tau_0)\, A_{\rm In}(\tau_0)\, d\tau_0, \quad (6)$$

where $A_{\rm In}(\tau)$ is the temporal complex amplitude of the input signal, and $\tilde{A}_{\rm Out}(\omega)$ is the spectral amplitude of the output signal. Assuming now illumination with totally incoherent light, the described system will be linear in intensity so that the intensity profile of the output signal spectrum, averaged over multiple realizations of the same process, will then be given by a superposition of the resulting intensity spectrum $|\tilde{A}_P(\omega, \tau_0)|^2$ from each temporal impulse of the input signal intensity profile [35],

[36]:

$$\begin{aligned}\left\langle \tilde{I}_{\mathrm{Out}}(\omega)\right\rangle &\propto \int_{-\infty}^{\infty}\left|\tilde{A}_P(\omega,\tau_0)\right|^2 |A_{\mathrm{In}}(\tau_0)|^2\, d\tau_0 \\ &\propto I_{\mathrm{In}}\left(-\ddot{\Phi}_{\mathrm{ID}}\omega\right)\otimes\left|P\left(\ddot{\Phi}_{\mathrm{ID}}\omega\right)\otimes h_{\mathrm{ID}}\left(\ddot{\Phi}_{\mathrm{ID}}\omega\right)\right|^2,\end{aligned} \tag{7}$$

where $\tilde{I}_{\mathrm{Out}}(\omega)=[\tilde{A}_{\mathrm{Out}}(\omega)]^2$ and $I_{\mathrm{In}}(\tau)=[A_{\mathrm{In}}(\tau)]^2$ hold for the intensity profiles of the output spectrum and input temporal waveform, respectively, and $\langle . \rangle$ denotes averaging over multiple realizations.

The condition of totally incoherent light implies an energy spectrum of infinite extent, which is practically not possible. In practice, to ensure that the optical wavefield is still incoherent after intensity modulation, the input temporal waveform and the time-domain pinhole should be much longer than the coherence time of the incoherent light source. For simplicity, the temporal pinhole is assumed to be implemented by a Gaussian short temporal modulation; in particular, $P(\tau)=\exp[-2\ln 2(\tau/\Delta T_P)^2]$ is the amplitude-transmittance function of the temporal pinhole, with ΔT_P being the intensity full width at half maximum (FWHM) of the pinhole profile. These conditions can be mathematically expressed as follows [35]

$$\delta\tau_{\mathrm{In}} \gg \tau_c \approx \frac{1}{\Delta f_{\mathrm{Source}}}, \tag{8}$$

$$\Delta T_P \gg \tau_c \approx \frac{1}{\Delta f_{\mathrm{Source}}}, \tag{9}$$

where $\delta\tau_{\mathrm{In}}$ represents the fastest time feature of the input waveform, τ_c is the coherence time of the incoherent light, and $\Delta f_{\mathrm{Source}}$ is an estimate of the full frequency bandwidth of the incoherent light source.

Eq. (7) confirms that the averaged output spectrum is proportional to the input temporal intensity profile, with a time-to-frequency scaling factor defined by the input dispersion value:

$$\omega = -\frac{\tau}{\ddot{\Phi}_{\mathrm{ID}}}. \tag{10}$$

Additionally, the scaled input temporal profile is convolved with the function $|P(\ddot{\Phi}_{\mathrm{ID}}\omega)\otimes h_{\mathrm{ID}}(\ddot{\Phi}_{\mathrm{ID}}\omega)|^2$, which can then be considered as the temporal impulse response of the incoherent-light linear system mapped into the frequency domain. This impulse response essentially determines the output spectral resolution of the time-to-frequency mapping process. In particular, this resolution can be estimated as the FWHM of $|P(\ddot{\Phi}_{\mathrm{ID}}\omega)\otimes h_{\mathrm{ID}}(\ddot{\Phi}_{\mathrm{ID}}\omega)|^2$.

The function $P(\ddot{\Phi}_{\mathrm{ID}}\omega)\otimes h_{\mathrm{ID}}(\ddot{\Phi}_{\mathrm{ID}}\omega)$ is essentially a Fresnel integral, and as such, it can be greatly simplified for the cases of a temporally short pinhole and a temporally long pinhole. The "Appendix" at the end of the paper shows a detailed mathematical analysis of a generic Fresnel integral, such as that of the above function, which is analytically solved for the two mentioned approximations of interest. In particular, the short-pinhole approximation holds when $P(\tau)$ is confined to a time width shorter than $2\Delta\tau$, i.e., $|\tau|\le\Delta\tau$, so that

$$\left|\frac{1}{2\ddot{\Phi}_{\mathrm{ID}}}\Delta\tau^2\right| \ll \pi. \tag{11}$$

Under this assumption, the Fresnel integral approaches the Fourier transform of the temporal pinhole (Fraunhofer approximation) and as a result, Eq. (7) can be approximated by

$$\left\langle \tilde{I}_{\mathrm{Out}}(\omega)\right\rangle \propto I_{\mathrm{In}}\left(-\ddot{\Phi}_{\mathrm{ID}}\omega\right)\otimes \tilde{I}_{\mathrm{Pinhole}}(\omega), \tag{12}$$

where $\tilde{I}_{\mathrm{Pinhole}}(\omega)=[\tilde{P}(\omega)]^2$ and $\tilde{P}(\omega)=\mathscr{F}[P(\tau)]$ hold for the intensity profile and the amplitude of the Fourier transform of the temporal pinhole, respectively. Thus, in this case, the output spectral resolution can be estimated as the intensity FWHM of $\tilde{I}_{\mathrm{Pinhole}}(\omega)$; for the assumed Gaussian pinholes, the resolution is:

$$\delta_{\omega,\mathrm{out}} \approx 4\ln 2/\Delta T_P. \tag{13}$$

Based on the time-to-frequency scaling factor in Eq. (10), the corresponding input temporal resolution is given by

$$\delta_{\tau,\mathrm{in}} \approx 4\ln 2\left|\ddot{\Phi}_{\mathrm{ID}}\right|/\Delta T_P. \tag{14}$$

On the other hand, the long-pinhole approximation holds when the pinhole spectrum $\tilde{P}(\omega)$ is confined to a bandwidth smaller than $2\Delta\omega$, i.e., $|\omega|\le\Delta\omega$, so that

$$\left|-\frac{\ddot{\Phi}_{\mathrm{ID}}}{2}\Delta\omega^2\right| \ll \pi. \tag{15}$$

In this case, the Fresnel integral is proportional to a scaled version of the temporal pinhole itself (Rayleigh range approximation), and Eq. (7) can be approximated by

$$\left\langle \tilde{I}_{\mathrm{Out}}(\omega)\right\rangle \propto I_{\mathrm{In}}\left(-\ddot{\Phi}_{\mathrm{ID}}\omega\right)\otimes I_{\mathrm{Pinhole}}\left(\ddot{\Phi}_{\mathrm{ID}}\omega\right), \tag{16}$$

where $I_{\mathrm{Pinhole}}(\tau)=[P(\tau)]^2$ holds for the intensity profile of the temporal pinhole. From Eq. (16), it can be inferred that the output spectral resolution is given by the intensity FWHM of $I_{\mathrm{Pinhole}}(\ddot{\Phi}_{\mathrm{ID}}\omega)$:

$$\delta_{\omega,\mathrm{out}} \approx \Delta T_P/\left|\ddot{\Phi}_{\mathrm{ID}}\right|, \tag{17}$$

and the corresponding input temporal resolution can be scaled as

$$\delta_{\tau,\mathrm{in}} \approx \Delta T_P. \tag{18}$$

Fig. 2 shows the numerically simulated relationship between the input temporal resolution and the intensity FWHM of the temporal pinhole (black circles), assuming that the temporal pinhole has a Gaussian profile [see Fig. 2(b)], and that the input dispersion is $\ddot{\Phi}_{\mathrm{ID}}=882.5$ ps^2 (-692 ps/nm). The dispersion value matches that used in experiments [32]. As illustrated in Fig. 2(a), Eqs. (14) and (18) provide a good approximation of the input temporal resolution for the cases of a temporally short pinhole (red solid line) and a long pinhole (blue short-dashed line), respectively. The optimal resolution is approximately achieved at the point of coincidence of the two curves defined by Eqs. (14) and (18). Thus, the optimal intensity FWHM time-width of the Gaussian pinhole is then

$$\Delta T_P \approx 2\sqrt{\ln 2\left|\ddot{\Phi}_{\mathrm{ID}}\right|}. \tag{19}$$

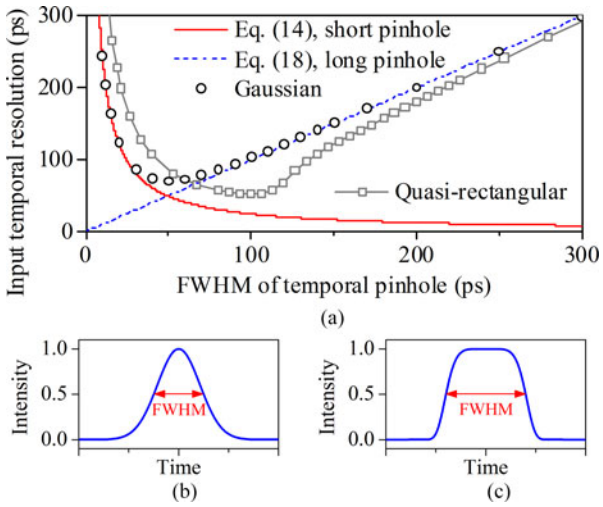

Fig. 2. Resolution characteristic of an incoherent-light time-to-frequency mapping system with the parameters defined in the text. The output spectral resolution is estimated as the intensity FWHM of the frequency-domain pulse that is obtained at the system output in response to an ideal temporal impulse; the corresponding input temporal resolution is obtained by scaling with the time-to-frequency mapping factor. (a) Numerically simulated resolutions assuming a temporal pinhole with a Gaussian shape (circles) and with a quasi-rectangular shape (squares and grey line), and the analytical approximations for the case of a short Gaussian-like temporal pinhole [solid red thin curves, Eq. (14)] and a long Gaussian-like temporal pinhole [dotted blue curves, Eq. (18)]. (b) Illustration of a Gaussian-like pinhole used in numerical simulations. (c) Illustration of a quasi-rectangular pinhole used in numerical simulation and experiments. In the numerical simulation, the quasi-rectangular pinhole is estimated as a third-order super-Gaussian function, which is used to approximate a physically realizable rectangular-like pulse, such as that used in experiments.

In this case, the output spectral resolution and input temporal resolution in the system can be respectively estimated from Eqs. (13) and (14), or from Eqs. (17) and (18). Clearly, the input temporal resolution offered by the pinhole-based time-to-frequency mapping system is limited by the temporal pinhole duration.

The resolution of the time-to-frequency mapping system also depends on the shape of the temporal pinhole and for instance, it can be slightly improved by using a quasi-rectangular (super-Gaussian) pinhole, as shown by results in Fig. 2 (grey line and squares). Fig. 2(b) and (c) shows the intensity profiles of a Gaussian-like pinhole and a quasi-rectangular pinhole. In the numerical simulation, the quasi-rectangular pinhole is estimated as a third-order super-Gaussian function, $P(\tau) = \exp[-2^{2m-1}\ln 2(\tau/\Delta T_P)^{2m}]$, where $m = 3$ is the order, and ΔT_P is the intensity FWHM of the super-Gaussian function.

Fig. 3(a) shows the normalized peak intensity of the output spectral pulse for input Gaussian pulses of different time-widths, assuming the above-defined dispersion value. The numerically simulated results (circles) and corresponding experimental values (squares) are compared with the theoretically calculated transmission characteristic (blue line), in which the output spectra are computed using Eq. (7). In the calculation and experiment, the temporal pinhole has a quasi-rectangular profile with an intensity FWHM of ∼146 ps, as shown in Fig. 2(c). The

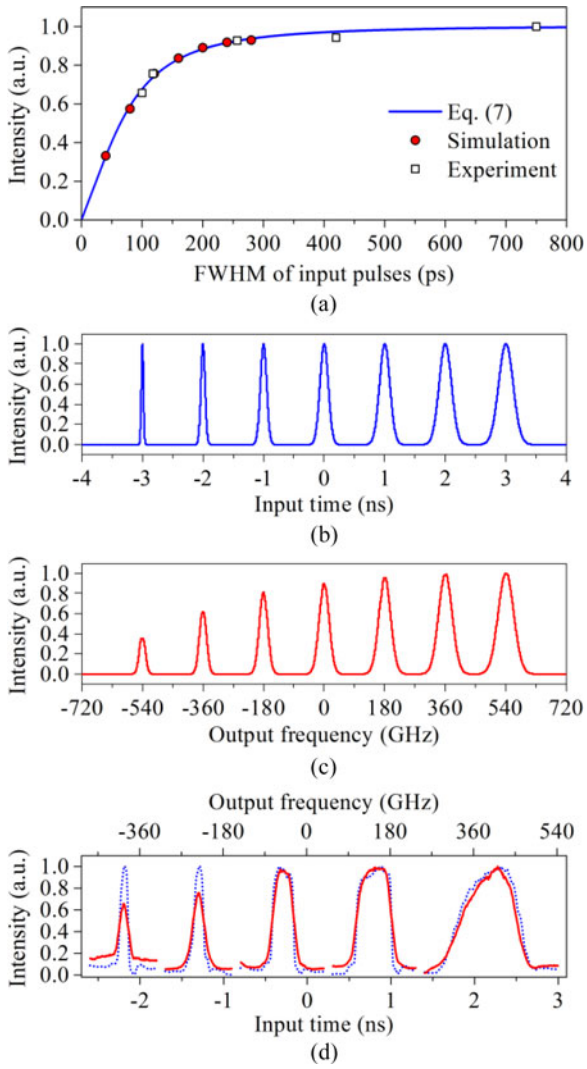

Fig. 3. (a) Theoretical, simulated and experimental transmission characteristic of an incoherent-light time-to-frequency mapping system with the parameters defined in the text (same parameters as in Fig. 2). For example, if the input of the system is a sequence of Gaussian pulses with different intensity FWHM time-widths, as shown in (b), the corresponding output frequency pulses will exhibit a decreased peak intensity as the input pulse width is shortened below the system resolution level, see (c). Note that (b) and (c) are numerically simulated results. (d) Experimentally measured traces corresponding to the output spectrum (solid red) compared with the scaled original temporal waveform (dotted blue), in which the scaling is fixed to be −692 ps/nm.

system transmission is reduced as the input pulse width is decreased. For example, the numerical results in Fig. 3(b) and (c) show that if a sequence of Gaussian pulses with different time-widths are input in the system [see Fig. 3(b)], the corresponding output pulses will exhibit a smaller peak intensity as the input time-width is decreased below the system resolution level, as shown in Fig. 3(c). Experimental results [32] corresponding to Fig. 3(a) are shown in Fig. 3(d) to illustrate examples of the system transmission. Experimental details of the system for these data can be found in [32]. In particular, the input resolution for the analyzed system is estimated to be ∼118 ps (from Eq. (7), results in Fig. 2), for which the corresponding spectral transmission in Fig. 3 exceeds ∼72%.

Another key performance specification of a temporal imaging system is the "temporal field of view," which is defined as the duration of the finite window over which the intended temporal-imaging operation can be performed. In an ideal system, the white-noise light source has a uniform (infinite-bandwidth) energy spectrum, and this would translate into a corresponding temporal field of view of infinite duration. However, for a practical incoherent light source with a limited frequency bandwidth, the time-to-frequency mapping process, and the related temporal imaging process, can be only realized along a limited temporal field of view [4]. As illustrated in Fig. 1(c), to ensure that some energy of the dispersed light can pass through the temporal pinhole, the input impulse must be within a certain time window, resulting in the following temporal field of view [4], [13]

$$T_A \approx 2\pi \left|\ddot{\Phi}_{\mathrm{ID}}\right| \Delta f_{\mathrm{Source}}, \tag{20}$$

where $\Delta f_{\mathrm{Source}}$ is the full-width optical bandwidth of the incoherent light source. Interestingly, the proposed system *inherently* implements time gating of the incoming optical waveform over the defined temporal field of view around a reference time defined by the pinhole timing, as the incoming light beyond this time window is filtered out. This intrinsic gating process avoids the need for an additional intensity time modulation process aimed at gating a potential continuous-time incoming signal. Additionally, this mechanism could be eventually exploited for the realization of the target time-to-frequency mapping process, and the related temporal imaging, in a continuous-time fashion [37].

B. Incoherent-Light Temporal Imaging

The temporal impulse response of the incoherent-light temporal imaging system in Fig 1(a) can be derived following a similar approach to that used for the first part of the system (time-to-frequency conversion process) in Section II-A above, first assuming a totally incoherent light source.

According to Fig. 1(b) and following the derivations from Eq. (5), the output temporal amplitude of the signal after the second (output) dispersion when a temporal impulse at τ_0 is input into the system can be obtained by

$$\begin{aligned} A_{\mathrm{OD}}(\tau,\tau_0) &= A_P(\tau,\tau_0) \otimes h_{\mathrm{OD}}(\tau) \\ &= \{P(\tau)[\delta(\tau-\tau_0)\otimes h_{\mathrm{ID}}(\tau)]\} \otimes h_{\mathrm{OD}}(\tau) \\ &= h_{0,\mathrm{ID}} h_{0,\mathrm{OD}} \exp\left(j\frac{1}{2\ddot{\Phi}_{\mathrm{ID}}}\tau_0^2\right) \exp\left(j\frac{1}{2\ddot{\Phi}_{\mathrm{OD}}}\tau^2\right) \\ &\quad \times \int_{-\infty}^{\infty} \exp\left[-j\tau_1\left(\frac{\tau_0}{\ddot{\Phi}_{\mathrm{ID}}}+\frac{\tau}{\ddot{\Phi}_{\mathrm{OD}}}\right)\right] P(\tau_1) \\ &\quad \times \exp\left(\frac{j\tau_1^2}{2\ddot{\Phi}_{\mathrm{Eff}}}\right) d\tau_1 = \frac{h_{0,\mathrm{ID}} h_{0,\mathrm{OD}}}{h_{0,\mathrm{Eff}}} \\ &\quad \times \exp\left\{\frac{j}{2}\left[\frac{\tau_0^2}{\ddot{\Phi}_{\mathrm{ID}}}+\frac{\tau^2}{\ddot{\Phi}_{\mathrm{OD}}}-\frac{\ddot{\Phi}_{\mathrm{Eff}}}{\ddot{\Phi}_{\mathrm{ID}}^2}(\tau_0-\tau_{\mathrm{TI}})^2\right]\right\} \\ &\quad \times \left[P\left[(\tau_0-\tau_{\mathrm{TI}})/\ddot{\Phi}_{\mathrm{ID}}\right] \otimes h_{\mathrm{Eff}}\left[(\tau_0-\tau_{\mathrm{TI}})/\ddot{\Phi}_{\mathrm{ID}}\right]\right], \end{aligned} \tag{21}$$

where $h_{\mathrm{OD}}(\tau) = h_{0,\mathrm{OD}} \exp[(j\tau^2)/(2\ddot{\Phi}_{\mathrm{OD}})]$ is the temporal complex envelope of the impulse response function of the output dispersion, with $\ddot{\Phi}_{\mathrm{OD}}$ being the group-delay dispersion, $h_{0,\mathrm{OD}} = 1/\sqrt{j2\pi\ddot{\Phi}_{\mathrm{OD}}}$, $\ddot{\Phi}_{\mathrm{Eff}}$ is defined as an effective group-delay dispersion, $1/\ddot{\Phi}_{\mathrm{Eff}} = (1/\ddot{\Phi}_{\mathrm{ID}}) + (1/\ddot{\Phi}_{\mathrm{OD}})$, $h_{\mathrm{Eff}}(\tau) = h_{0,\mathrm{Eff}} \exp[(j\tau^2)/(2\ddot{\Phi}_{\mathrm{Eff}})]$ is the impulse response function envelope corresponding to this effective dispersion, $h_{0,\mathrm{Eff}} = 1/\sqrt{j2\pi\ddot{\Phi}_{\mathrm{Eff}}}$, and $\tau_{\mathrm{TI}} = -(\ddot{\Phi}_{\mathrm{ID}}\tau)/\ddot{\Phi}_{\mathrm{OD}}$.

As shown by Eq. (21), apart from the quadratic phase preceding the convolution, $A_{\mathrm{OD}}(\tau,\tau_0)$, i.e., the coherent temporal impulse response of the pinhole system under analysis, depends only on the difference in $\tau_0 - \tau_{\mathrm{TI}}$. Assuming a coherent input optical waveform, $A_{\mathrm{In}}(\tau)$, the temporal complex envelope of the output signal can be calculated as follows:

$$A_{\mathrm{Out}}(\tau) = \int_{-\infty}^{\infty} A_{\mathrm{OD}}(\tau,\tau_0)\, A_{\mathrm{In}}(\tau_0)\, d\tau_0. \tag{22}$$

where $A_{\mathrm{Out}}(\tau)$ is the temporal complex amplitude of the output signal. Assuming further illumination with a totally incoherent light source, the averaged intensity profile of the output signal is then given by a superposition of the intensity contributions from each of the temporal impulses of the input waveform [35], [36]:

$$\begin{aligned} \langle I_{\mathrm{Out}}(\tau)\rangle &\propto \int_{-\infty}^{\infty} |A_{\mathrm{OD}}(\tau,\tau_0)|^2 I_{\mathrm{In}}(\tau_0)\, d\tau_0 \\ &\propto I_{\mathrm{In}}\left(-\frac{\ddot{\Phi}_{\mathrm{ID}}}{\ddot{\Phi}_{\mathrm{OD}}}\tau\right) \otimes \left|P\left(\frac{\ddot{\Phi}_{\mathrm{Eff}}}{\ddot{\Phi}_{\mathrm{OD}}}\tau\right) \otimes h_{\mathrm{Eff}}\left(\frac{\ddot{\Phi}_{\mathrm{Eff}}}{\ddot{\Phi}_{\mathrm{OD}}}\tau\right)\right|^2 \end{aligned} \tag{23}$$

where $I_{\mathrm{Out}}(\tau) = [A_{\mathrm{Out}}(\tau)]^2$ holds for the intensity profile of the output waveform. In practice, Eq. (23) is valid under the conditions defined by Eqs. (8) and (9) above concerning the coherence time of the used light source. As predicted, Eq. (23) confirms that the averaged output intensity is a temporally scaled replica of the input intensity profile, with the temporal magnification factor given by

$$M = -\frac{\ddot{\Phi}_{\mathrm{OD}}}{\ddot{\Phi}_{\mathrm{ID}}}. \tag{24}$$

Additionally, the scaled input replica is temporally convolved with the function, $|P(\frac{\ddot{\Phi}_{\mathrm{Eff}}}{\ddot{\Phi}_{\mathrm{OD}}}\tau) \otimes h_{\mathrm{Eff}}(\frac{\ddot{\Phi}_{\mathrm{Eff}}}{\ddot{\Phi}_{\mathrm{OD}}}\tau)|^2$, which represents then the temporal impulse response of the incoherent-light imaging system. This convolution process imposes a limited temporal resolution in the system, which can be estimated as the FWHM time-width of the impulse response, $|P(\frac{\ddot{\Phi}_{\mathrm{Eff}}}{\ddot{\Phi}_{\mathrm{OD}}}\tau) \otimes h_{\mathrm{Eff}}(\frac{\ddot{\Phi}_{\mathrm{Eff}}}{\ddot{\Phi}_{\mathrm{OD}}}\tau)|^2$.

The defined impulse response function is essentially a Fresnel integral and as such, this function and the related Eq. (23) can be greatly simplified for the cases of a temporally short pinhole and a temporally long pinhole. Detailed derivations on these two approximations for a Fresnel integral can be found in the "Appendix" at the end of the paper. In particular, if $P(\tau)$ is

confined to a time width shorter than $2\Delta\tau$, so that

$$\left|\frac{1}{2\ddot{\Phi}_{\mathrm{Eff}}}\Delta\tau^2\right| \ll \pi, \tag{25}$$

then, the Fresnel integral is proportional to the scaled Fourier transform of the pinhole temporal amplitude (Fraunhofer approximation) and Eq. (23) can be mathematically approximated by

$$\langle I_{\mathrm{Out}}(\tau)\rangle \propto I_{\mathrm{In}}\left(-\frac{\ddot{\Phi}_{\mathrm{ID}}}{\ddot{\Phi}_{\mathrm{OD}}}\tau\right) \otimes \tilde{I}_{\mathrm{Pinhole}}\left(\frac{\tau}{\ddot{\Phi}_{\mathrm{OD}}}\right). \tag{26}$$

From Eq. (26), the output temporal resolution can be estimated as the intensity FWHM of $\tilde{I}_{\mathrm{Pinhole}}(\tau/\ddot{\Phi}_{\mathrm{OD}})$:

$$\delta_{\tau,\mathrm{out}} \approx 4\ln 2\left|\ddot{\Phi}_{\mathrm{OD}}\right|/\Delta T_P. \tag{27}$$

Based on the system's temporal magnification factor, the corresponding input temporal resolution is then given by

$$\delta_{\tau,\mathrm{in}} \approx 4\ln 2\left|\ddot{\Phi}_{\mathrm{ID}}\right|/\Delta T_P. \tag{28}$$

Concerning the long-pinhole approximation, if the temporal pinhole spectrum, $\tilde{P}(\omega)$, is confined to a bandwidth smaller than $2\Delta\omega$ so that

$$\left|-\frac{\ddot{\Phi}_{\mathrm{Eff}}}{2}\Delta\omega^2\right| \ll \pi, \tag{29}$$

then, the Fresnel integral is proportional to the temporal pinhole waveform itself (Rayleigh range approximation), and Eq. (23) can be approximated by

$$\langle I_{\mathrm{Out}}(\tau)\rangle \propto I_{\mathrm{In}}\left(-\frac{\ddot{\Phi}_{\mathrm{ID}}}{\ddot{\Phi}_{\mathrm{OD}}}\tau\right) \otimes I_{\mathrm{Pinhole}}\left(\frac{\ddot{\Phi}_{\mathrm{ID}}}{\ddot{\Phi}_{\mathrm{ID}}+\ddot{\Phi}_{\mathrm{OD}}}\tau\right). \tag{30}$$

From Eq. (30), the output temporal resolution is given by the intensity FWHM of $I_{\mathrm{Pinhole}}[\ddot{\Phi}_{\mathrm{ID}}\tau/(\ddot{\Phi}_{\mathrm{ID}}+\ddot{\Phi}_{\mathrm{OD}})]$:

$$\delta_{\tau,\mathrm{out}} \approx \left|\frac{\ddot{\Phi}_{\mathrm{ID}}+\ddot{\Phi}_{\mathrm{OD}}}{\ddot{\Phi}_{\mathrm{ID}}}\right|\Delta T_P, \tag{31}$$

and the corresponding input temporal resolution is

$$\delta_{\tau,\mathrm{in}} \approx \left|\frac{\ddot{\Phi}_{\mathrm{ID}}+\ddot{\Phi}_{\mathrm{OD}}}{\ddot{\Phi}_{\mathrm{OD}}}\right|\Delta T_P. \tag{32}$$

Similarly to its coherent counterpart, the performance of an incoherent-light temporal imaging system can be described by its temporal resolution and temporal field of view. The later represents the time window over which the desired imaging process is implemented. These two parameters are typically defined at the point of highest resolution in the system, namely the input port for temporal magnification systems ($|M|>1$) and output port for temporal compression systems ($|M|<1$). The ratio between the output and input temporal resolutions (and temporal field of view) is defined by the magnification factor M. A main figure of merit of a temporal imaging system is the ratio between the temporal field of view and temporal resolution at the same port, typically refereed to as the time-bandwidth product of the system. As discussed in Section II-A above, the temporal field of view of the proposed imaging scheme at the input port is determined by the product of the light source bandwidth and input dispersion, Eq. (20), and time gating over this field of view is intrinsically implemented by the system around the pinhole reference time.

We recall that the approximations in Eq. (32) roughly corresponds to a direct projection of the temporal pinhole onto the output image, as expected for a pinhole duration that is sufficiently long to neglect the effect of dispersive propagation. The approximations in Eq. (28) corresponds to the opposite case, where a projection of the dispersion-induced temporal far-field (Fraunhofer) pattern of the pinhole is obtained onto the output image. Similarly to the time-to-frequency mapping case (see Section II-A), the optimal output temporal resolution is achieved at the point where the two approximations in Eqs. (28) and (32) coincide. Thus, the optimal FWHM time width of the pinhole is

$$\Delta T_{P,\mathrm{opt}} \approx 2\sqrt{\ln 2\left|\ddot{\Phi}_{\mathrm{ID}}\ddot{\Phi}_{\mathrm{OD}}/\left(\ddot{\Phi}_{\mathrm{ID}}+\ddot{\Phi}_{\mathrm{OD}}\right)\right|}, \tag{33}$$

and its corresponding output and input temporal resolutions can be respectively estimated by Eqs. (27) and (28), or (31) and (32), respectively. Fig. 4(a) shows the optimal pinhole time-width, and corresponding system resolution (input temporal resolution), and as a function of the magnification factor (M) for a temporal magnification system. The ratio of the system resolution and optimal pinhole time-width as a function of the magnification factor is shown in Fig. 4(b). Fig. 4(c) shows the system resolution (output temporal resolution) and the optimal pinhole time-width as a function of the compression factor ($= 1\ /\ M$) for a temporal compression system. The ratio of the system resolution and optimal pinhole time-width is shown in Fig. 4(d). The simulated designs in Fig. 4 are assumed to have the same input dispersion (-692 ps/nm) and a Gaussian temporal pinhole. Output dispersion is varied according to the specific magnification/compression factor.

Fig. 4 shows that the system resolution approaches a value slightly longer than the pinhole time-width for systems with high magnification/compression factors. However, as illustrated by the results in Fig. 4(b) and (d), for moderate to low magnification/compression factors, the system can be designed to provide a much higher resolution by using input and output dispersive elements of opposite signs (M being positive), see gray-shadow areas in the plots Fig. 4(b) and (d). Ideally, an infinite resolution ($\delta\tau_{\mathrm{In}} = 0$) can be achieved for the trivial case when $M = 1$, requiring an infinitely long temporal pinhole (in practice, the pinhole full time-width should just exceed the duration of the dispersed input waveform). Such an improvement is not available for spatial imaging, because diffraction in the space domain has only one sign. Additionally, similarly to the time-to-frequency mapping case, the resolution of the temporal imaging system is dependent on the profile of the temporal pinhole and in particular, it can be further improved by using a quasi-rectangular temporal pinhole.

The provided estimates for temporal resolution were numerically and experimentally validated. Fig. 5(a) shows the normalized peak intensity of the output temporal pulse as a function

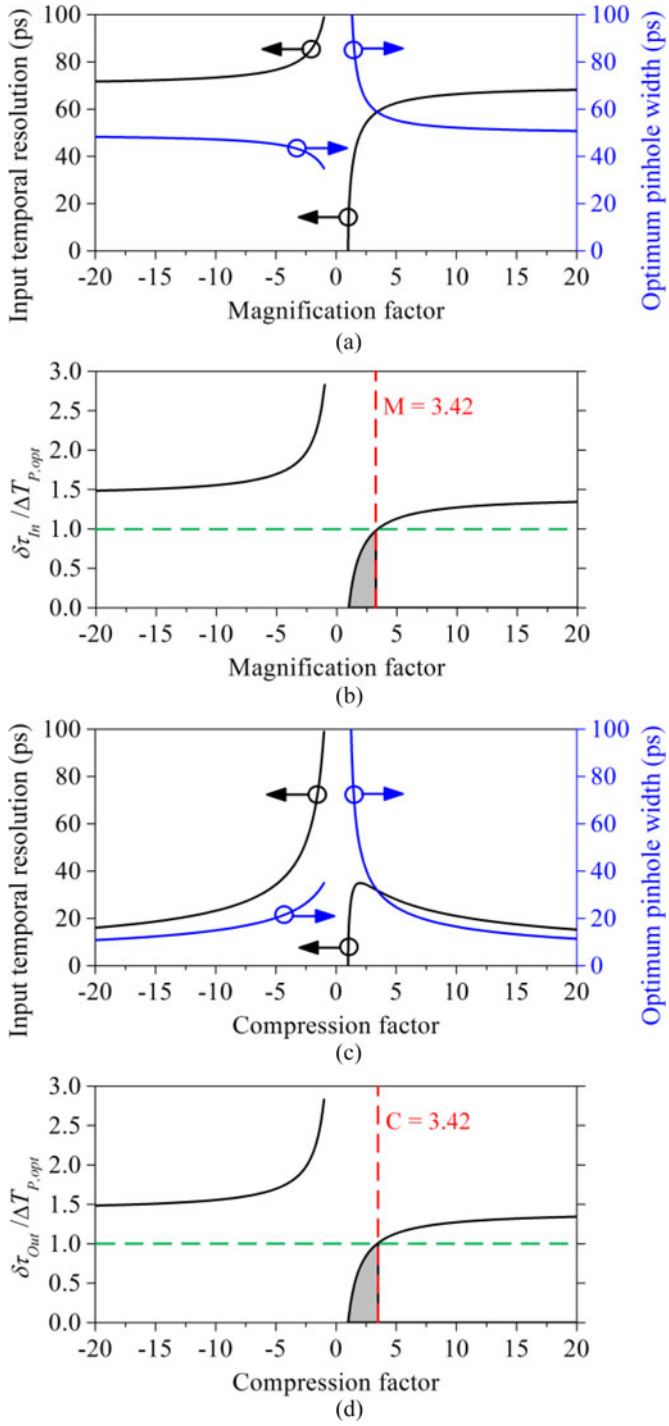

Fig. 4. Numerical results on system resolutions as a function of the magnification/compression factors for a temporal magnification system (a-b) and a temporal compression system (c-d). In the numerical simulation, we assume that the input dispersion is −692 ps/nm for both systems and the pinhole has a Gaussian profile. (a) System resolution (input temporal resolution) and optimal pinhole time-width as a function of the magnification factor (M) for a temporal magnification system with the parameters defined in the text. (b) Ratio of the input temporal resolution to optimal pinhole time-width as a function of the magnification factor for the same magnification system configuration. (c) System resolution (output temporal resolution) and the optimal pinhole time-width as a function of the compression factor ($= 1/M$) for a temporal compression system. (d) Ratio of the output temporal resolution to optimal pinhole time-width as a function of the compression factor for the same compression system configuration, where C is the compression factor.

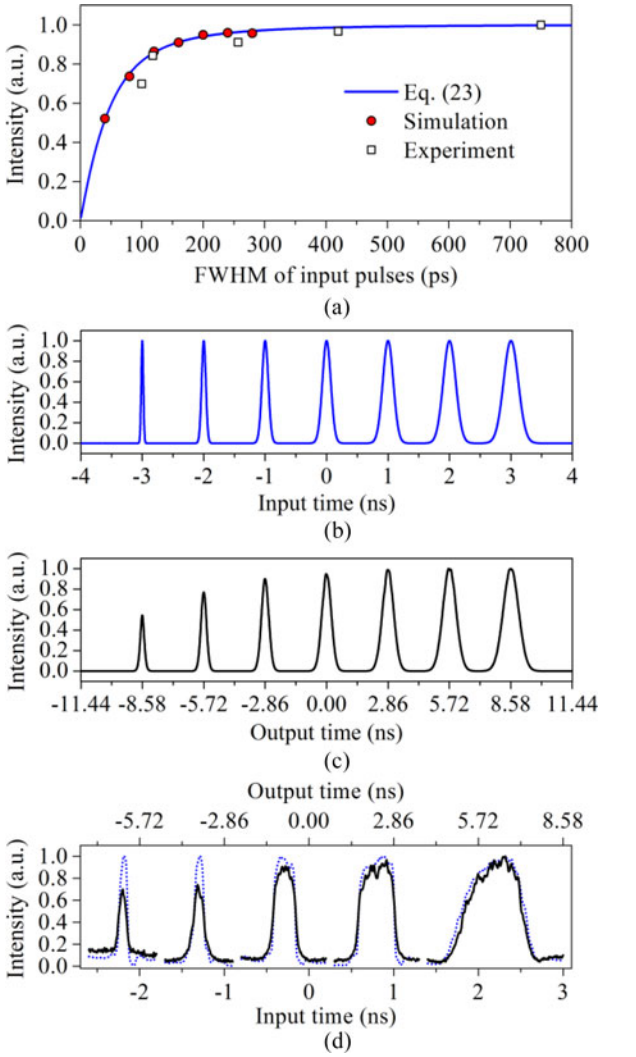

Fig. 5. (a) Theoretical, simulated and experimental transmission characteristic of an incoherent-light temporal imaging system with the parameters defined in the text (same as for Fig. 4). For example, if the input of the system is a sequence of Gaussian pulses with different intensity FWHM time-widths, as shown in (b), the corresponding output temporal pulses will exhibit a decreased peak intensity as the input pulse width is shortened below the system resolution level, see (c). Note that (b) and (c) are numerically simulated results. (d) Experimentally measured traces corresponding to the output temporal waveform (solid black) compared with the scaled original temporal waveform (dotted blue), in which the scaling is fixed to be $M = 2.86$.

of the input Gaussian pulse time-width for the temporal magnification system configuration defined above. The numerically simulated results (circles) and experimental values (squares) obtained in this way are compared with the theoretically calculated transmission characteristic (blue line); the later is computed using Eq. (23). In the calculation and experiment, the temporal pinhole has an approximate quasi-rectangular profile with an intensity FWHM of ∼146 ps, as shown in Figs. 2(c) and 8(c), and the input and output dispersion are −692 ps/nm (882.5 ps^2) and 1981 ps/nm (−2526.3 ps^2), respectively, implementing a temporal magnification factor of $M = 2.86$ (values from experimental results [32]). As illustrated in Fig. 5(a)–(d), the intensity transmission is deteriorated as the input pulse width decreases

below the corresponding resolution value. In particular, the numerically estimated input resolution for this system is ∼51 ps (from Eq. (23)), for which the normalized transmission still exceeds ∼55%.

C. Incoherent-Light Frequency-to-Time Mapping

As discussed in Section I, incoherent-light frequency-to-time mapping has been proposed and demonstrated by using a short temporal gate (or intensity temporal modulation driven by an electronic impulse) followed by a dispersive element [25]–[31]. In this paper, we interpret the short time gate as a temporal pinhole and provide a detailed mathematical study of the process, including a derivation of the system's impulse response and the related performance analysis, within the general framework introduced here.

Fig. 6(a) illustrates the incoherent-light frequency-to-time mapping process under study. A similar procedure to that reported in Sections II-A and II-B is followed here for calculation of the incoherent-light system impulse response. To obtain first the coherent impulse response, the input spectrum, which is realized by spectrally filtering the input light source, is assumed to be a spectral impulse at ω_0. The spectral amplitude of the input spectrum is thus given by

$$\tilde{A}_{\mathrm{In}}(\omega,\omega_0)=\delta(\omega-\omega_0). \tag{34}$$

The temporal amplitude of the light after propagating through the temporal pinhole is

$$A_P(\tau,\omega_0)=A_{\mathrm{In}}(\tau,\omega_0)\,P(\tau)=\mathscr{F}^{-1}\left[\tilde{A}_{\mathrm{In}}(\omega,\omega_0)\right]P(\tau) \tag{35}$$

where $A_0(\tau)$ is the temporal amplitude at the output of the light source. The modulated light is then sent through a dispersive element. The temporal amplitude after dispersion is given by

$$\begin{aligned}A_D(\tau,\omega_0) &= A_P(\tau,\omega_0)\otimes h(\tau)\\ &= \left\{\mathscr{F}^{-1}\left[\delta(\omega-\omega_0)\right]P(\tau)\right\}\otimes\left[h_0\exp\left(j\frac{1}{2\ddot{\Phi}}\tau^2\right)\right]\\ &= \frac{h_0}{\sqrt{2\pi}}\exp\left\{\frac{j}{2\ddot{\Phi}}\left[\tau^2-\left(\tau-\ddot{\Phi}\omega_0\right)^2\right]\right\}\int_{-\infty}^{\infty}P(\tau_1)\\ &\quad\times\exp\left\{j\frac{1}{2\ddot{\Phi}}\left[\left(\tau-\ddot{\Phi}\omega_0\right)-\tau_1\right]^2\right\}d\tau_1\\ &= \frac{1}{\sqrt{2\pi}}\exp\left[\frac{-j}{2\ddot{\Phi}}\left(\omega_F^2+2\tau\omega_F\right)\right]P(\tau-\tau_F)\\ &\quad\otimes h(\tau-\tau_F),\end{aligned} \tag{36}$$

where $h(\tau)=h_0\exp[(j\tau^2)/(2\ddot{\Phi})]$ is the complex envelope of the temporal impulse response function of the dispersive medium, $\ddot{\Phi}$ is group-delay dispersion, $h_0=1/\sqrt{j2\pi\ddot{\Phi}}$ [3], and $\tau_F=\ddot{\Phi}\omega_0$.

As shown by Eq. (36), apart from the quadratic phase preceding the convolution, $A_D(\tau,\omega_0)$, the temporal amplitude of the coherent temporal impulse response of the spectral impulse at ω_0, depends only on the difference in $\tau-\tau_F$. For a coherent system, when a coherent spectral waveform $\tilde{A}_{\mathrm{In}}(\omega)$ is input into the system, the temporal complex amplitude of the output signal is

$$A_{\mathrm{Out}}(\tau)=\int_{-\infty}^{\infty}A_D(\tau,\omega_0)\,\tilde{A}_{\mathrm{In}}(\omega_0)\,d\omega_0, \tag{37}$$

where $\tilde{A}_{\mathrm{In}}(\omega)$ is the spectral amplitude of the input signal. The incoherent-light assumption in this case implies that the phase relationships among the different spectral components of the input light source are totally uncorrelated, i.e., the frequency-domain autocorrelation function is a delta function. In this case, the averaged intensity temporal profile of the output signal is a superposition of contributions from each of the spectral impulses of the input spectrum [28], [35], [36], as follows:

$$\begin{aligned}\langle I_{\mathrm{Out}}(\tau)\rangle &\propto \int_{-\infty}^{\infty}|A_D(\tau,\omega_0)|^2\,\tilde{I}_{\mathrm{In}}(\omega_0)\,d\omega_0\\ &\propto \tilde{I}_{\mathrm{In}}\left(\frac{\tau}{\ddot{\Phi}}\right)\otimes|P(\tau)\otimes h(\tau)|^2,\end{aligned} \tag{38}$$

where $\tilde{I}_{\mathrm{In}}(\omega)=[\tilde{A}_{\mathrm{In}}(\omega)]^2$ holds for the intensity profile of the input spectrum. The above assumption on the incoherent light source is an ideal one. In practice, to ensure that the pinhole modulation process does not introduce undesired correlations among consecutive spectral components of the input light source, the pinhole time-width must be much longer than the coherence time of the filtered light source [35]:

$$\Delta T_P\gg\tau_c\approx\frac{1}{\delta f_{\mathrm{Sig}}}, \tag{39}$$

where τ_c is the coherence time of the incoherent light after spectrally filtering, δf_{Sig} is the fastest frequency feature of the input amplitude spectrum.

From Eq. (38), it can be inferred that the averaged temporal intensity profile at the system output is proportional to the input energy spectrum. The frequency-to-time mapping factor is given by

$$\omega=\frac{\tau}{\ddot{\Phi}}. \tag{40}$$

Moreover, at the system output, the scaled input spectrum is convolved with the function $|P(\tau)\otimes h(\tau)|^2$, which defines

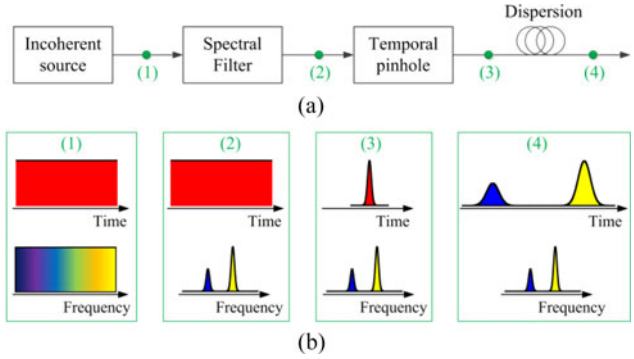

Fig. 6. Incoherent-light frequency-to-time mapping. (a) Diagram of an incoherent-light frequency-to-time mapping system. (b) The evolution of the signal along the frequency-to-time mapping system. In this example, the spectral filter consists of two Gaussian-like pulses of different amplitude. All waveforms and spectra are averaged profiles.

the linear impulse response of the frequency-to-time mapping system. The output temporal resolution of the incoherent-light frequency-to-time mapping process can then be estimated as intensity FWHM time-width of $|P(\tau) \otimes h(\tau)|^2$. This is again the squared magnitude of a Fresnel integral; in this case, this Fresnel integral has a very straightforward interpretation, namely the result of propagating the temporal pinhole waveform through the optical dispersive line. Hence, using the detailed derivations in the Appendix, Eq. (38) can be again greatly simplified for the cases of a short temporal pinhole (Fraunhofer approximation) and a long pinhole (Rayleigh range approximation). In the first case, if the pinhole $P(\tau)$ is confined to a time width shorter than $2\Delta\tau$ so that

$$\left|\frac{1}{2\ddot{\Phi}}\Delta\tau^2\right| \ll \pi, \tag{41}$$

then the dispersed pinhole is proportional to the spectrum of the input temporal pinhole and in particular, Eq. (38) can be approximated by

$$\langle I_{\mathrm{Out}}(\tau)\rangle \propto \tilde{I}_{\mathrm{In}}\left(\frac{\tau}{\ddot{\Phi}}\right) \otimes \tilde{I}_{\mathrm{Pinhole}}\left(\frac{\tau}{\ddot{\Phi}}\right). \tag{42}$$

Therefore, in this case, the output temporal resolution is estimated as the intensity FWHM of $\tilde{I}_{\mathrm{Pinhole}}\left(\tau/\ddot{\Phi}\right)$:

$$\delta_{\tau,\mathrm{out}} \approx 4\ln 2\left|\ddot{\Phi}\right|/\Delta T_P, \tag{43}$$

and using the frequency-to-time scaling in Eq. (40), the corresponding input spectral resolution is given by

$$\delta_{\omega,\mathrm{in}} \approx 4\ln 2/\Delta T_P. \tag{44}$$

In the long-pinhole case, if the pinhole spectrum $\tilde{P}(\omega)$ is confined to a bandwidth smaller than $2\Delta\omega$ so that

$$\left|-\frac{\ddot{\Phi}}{2}\Delta\omega^2\right| \ll \pi, \tag{45}$$

then the pinhole propagates through the output dispersive medium without undergoing any notable distortion and equation (38) can be approximated by

$$\langle I_{\mathrm{Out}}(\tau)\rangle \propto \tilde{I}_{\mathrm{In}}\left(\frac{\tau}{\ddot{\Phi}}\right) \otimes I_{\mathrm{Pinhole}}(\tau). \tag{46}$$

The output temporal resolution is then given by the intensity FWHM of $I_{\mathrm{Pinhole}}(\tau)$:

$$\delta_{\tau,out} \approx \Delta T_P, \tag{47}$$

and the corresponding input spectral resolution can be scaled as

$$\delta_{\omega,\mathrm{in}} \approx \Delta T_P/\left|\ddot{\Phi}\right|. \tag{48}$$

The optimal temporal resolution is again approximately achieved at the point of coincidence of the two curves defined by Eqs. (43) and (47). Thus, the optimal intensity FWHM time-width of the pinhole is then

$$\Delta T_P \approx 2\sqrt{\ln 2\left|\ddot{\Phi}\right|}. \tag{49}$$

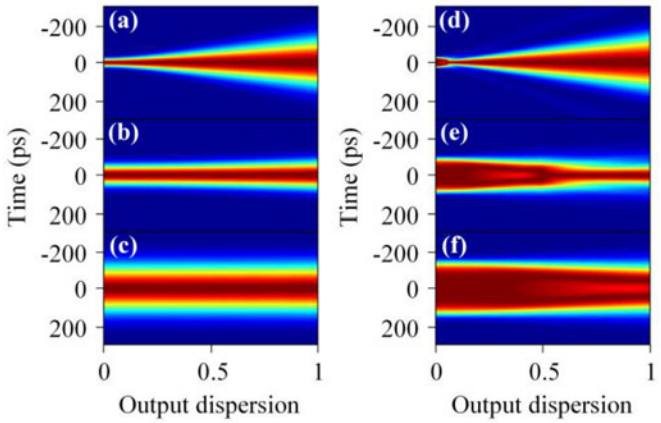

Fig. 7. Resolution characteristic of an incoherent-light frequency-to-time mapping system. (a)–(c) The evolution of the optical wave along the dispersive medium when using Gaussian temporal pinholes with intensity FWHM time-widths of 35 ps [(a) short pinhole approximation], 83.7 ps [(b) optimal temporal pinhole], and 200 ps [(c) long pinhole approximation], respectively. (d)–(f) The evolution of the optical wave along the dispersive medium when using quasi-rectangular temporal profiles with intensity FWHM time-widths of 53.2 ps [(d) short temporal pinhole approximation], 173 ps [(e) optimal temporal pinhole approximation], and 278.8 ps [(f) long temporal pinhole approximation], respectively.

In this case, the output temporal resolution and input spectral resolution in the system can be respectively estimated from Eqs. (43) and (44), or from Eqs. (47) and (48), respectively. The output temporal resolution is ultimately limited by the pinhole duration, Eq. (47). To be more concrete, if the temporal pinhole duration is fixed to its optimal value, Eq. (49), the input frequency resolution, Eq. (48), will be improved using a higher optical dispersion, proportionally to the squared root of the dispersion value. This trend is in agreement with previously derived conditions on the frequency resolution of the input signal spectrum versus dispersion [27].

The frequency-to-time mapping process provides a very intuitive ground to get a deeper insight into the temporal pinhole optimization issue for imaging systems based on a pinhole. Fig. 7(a)–(c)show the evolution of the optical wave along the dispersive medium for Gaussian temporal pinholes with intensity FWHM time-widths of 35 ps [(a) short pinhole approximation], 83.7 ps [(b) optimal temporal pinhole], and 200 ps [(c) long pinhole approximation], respectively. In the numerical simulation, a spectral impulse given by Eq. (34) is launched so that the system resolution can be estimated as the temporal width of the output pulse. As discussed above, the approximation in Eq. (43), illustrated in Fig. 7(a), corresponds to the case where a projection of the dispersion-induced temporal far-field (Fraunhofer) pattern of the pinhole is obtained onto the output image. The approximation in Eq. (47), illustrated in Fig. 7(c), corresponds to a direct projection of the temporal pinhole onto the output image, as expected for a pinhole duration that is sufficiently long to neglect the effect of dispersive propagation. The optimal pinhole duration is obtained for the shortest time-width that can still propagate through the dispersive medium with nearly negligible distortion (spread), Fig. 7(b). As for any

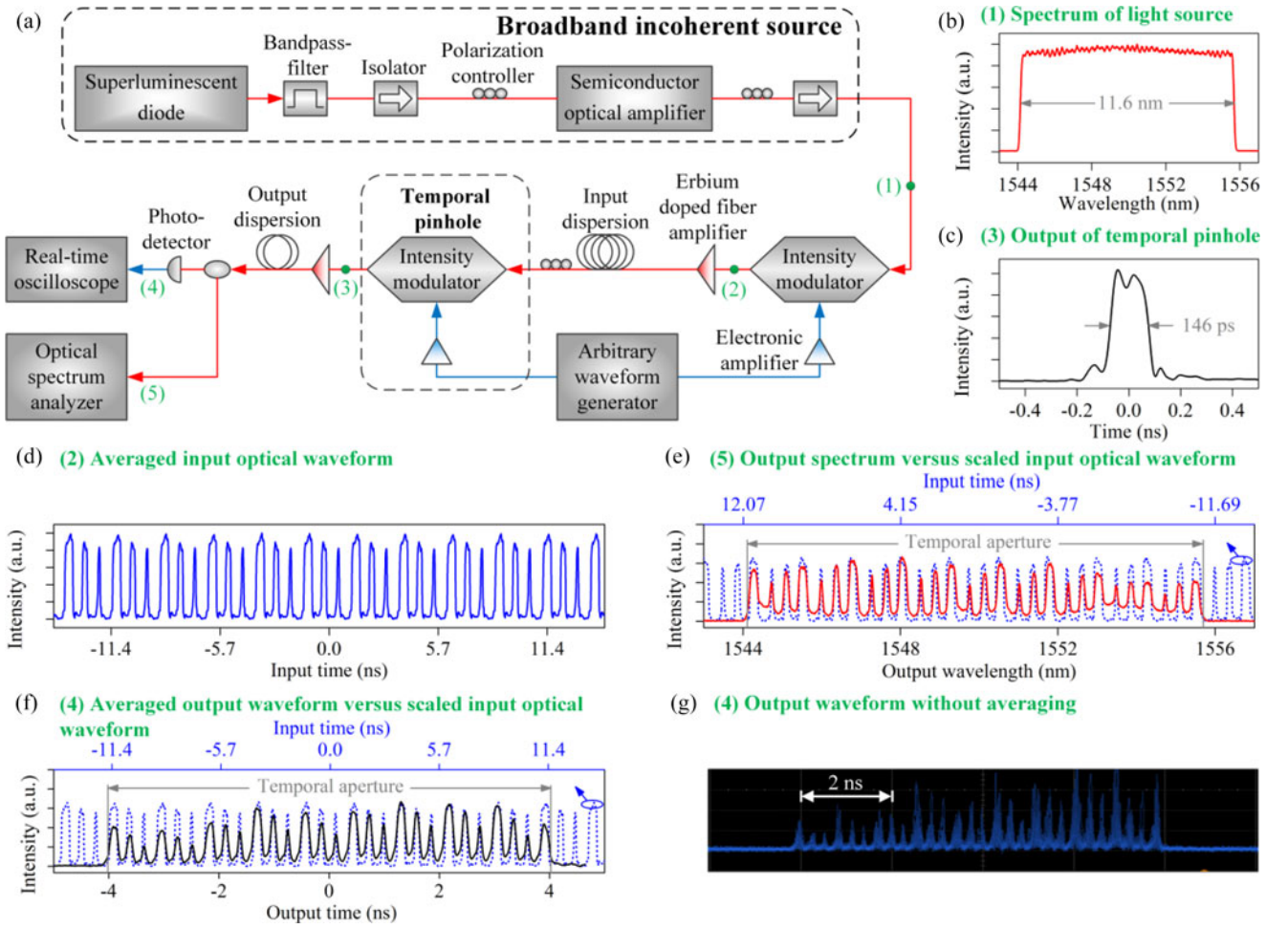

Fig. 8. Experimental setup and output waveforms along an incoherent-light temporal imaging (compression) system. (a) Experimental setup of the incoherent-light temporal imaging system. (b) Spectrum of the broadband incoherent light source. (c) Optical output from the temporal pinhole. (d) Input optical temporal waveform. (e) Spectrum (solid red curve) of the output image compared with the input temporal waveform (dashed blue curve), where the scaling between input time and normalized output wavelength (with respect to the signal's central optical wavelength) is the predicted time-to-frequency mapping factor, −1981 ps/nm. (f) Temporal intensity profile (solid black curve) of the output image compared with the scaled input temporal waveform (dashed blue curve), where the scaling between input time and output time is the predicted magnification factor $M = 1/2.86$. All profiles in (b)–(f) are averaged for 256 times. (g) Temporal intensity profile of the output image without averaging.

temporal imaging system based on a pinhole, the resolution of the frequency-to-time mapping system also depends on the shape of the temporal pinhole and in particular, it can be further improved by using a quasi-rectangular pinhole, Fig. 7(d)–(f) illustrates the evolution of the optical wave along the dispersive medium when the used temporal pinholes have quasi-rectangular profiles with intensity FWHM time-widths of 53.2 ps [(d) short temporal pinhole], 173 ps [(e) optimal temporal pinhole], and 278.8 ps [(f) long temporal pinhole], respectively. Although the optimal quasi-rectangular temporal pinhole has a larger intensity FWHM time-width than the optimal Gaussian temporal pinhole, the output temporal resolution for the optimal quasi-rectangular temporal pinhole [see Fig. 7(e)] is higher than that for the optimal Gaussian temporal pinhole [see Fig. 7(b)]. Essentially, in the optimal case, the quasi-rectangular pinhole undergoes a "temporal compression" of its main energy lobe that does not occur for the Gaussian pinhole case.

III. Experimental Results

The incoherent-light scheme under study here has been recently demonstrated for temporal stretching (magnification) of intensity RF waveforms [32]. For completeness, this paper presents a set of complementary experimental results to demonstrate the capability of the scheme for performing temporal compression and time-to-frequency mapping of intensity waveforms.

A. Incoherent-Light Temporal Compression

Fig. 8(a) shows the experimental setup used for demonstration of incoherent-light temporal compression. Broadband incoherent light with a nearly uniform spectrum is generated by spectrally filtering the optical radiation from a superluminescent diode (∼2 mW average power and ∼80 nm bandwidth) followed by amplification with a semiconductor optical

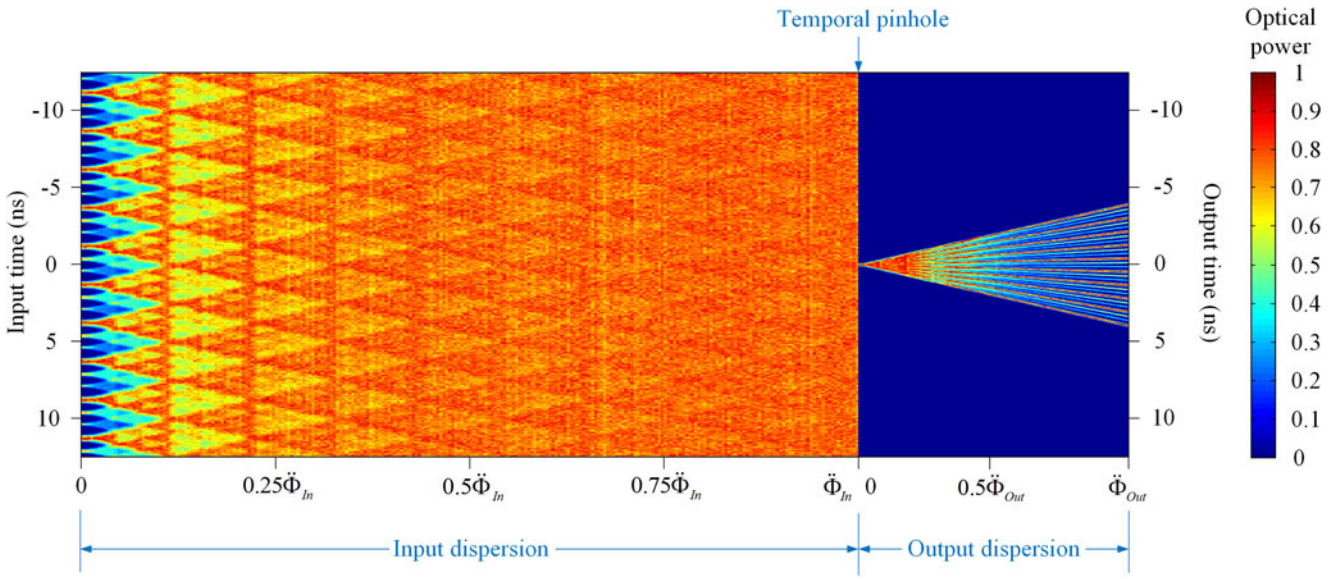

Fig. 9. Numerically calculated carpet for incoherent-light temporal compression. The carpet illustrates the evolution of the signal along the experimentally demonstrated temporal compression system in Fig. 8. The color bar to the right of the plot shows the relationship between colors and the signal optical power.

amplifier (SOA). The SOA is set to provide an optical gain of ∼26.8 dBm, a saturation power of ∼15.5 dBm and a bandwidth of ∼80.6 nm. The used spectral filter has a rectangular-like profile, centered at a wavelength of 1549.9 nm, with an intensity FWHM wavelength bandwidth of ∼11.6 nm. The two fiber-optic isolators in the incoherent light source have bandwidths of ∼43 and ∼100 nm, respectively. The wavelength spectrum of the constructed broadband incoherent light source is presented in Fig. 8(b), showing a full-width bandwidth of ∼11.6 nm. As shown in Fig. 8(a), the input incoherent optical signal to be imaged is obtained by intensity modulation of the broadband incoherent light with the RF temporal waveform under analysis, using a 40-GHz electro-optic intensity modulator. The modulating RF signal is generated by a 12-GHz electronic arbitrary waveform generator and then amplified by a 12-GHz electronic amplifier. For the example reported here, the input signal, shown in Fig. 8(d), is a periodic train of Gaussian-like pulses of different time widths. The three different consecutive pulses in the input sequence have FWHM time widths of 420, 257 and 118 ps, respectively. The periodic time separations between these three pulses are 0.83 and 0.75 ns, respectively. The modulated light is then sent through the input dispersive line, which introduces a dispersion of +1981 ps/nm, and the temporal pinhole. The temporal pinhole is realized by another 40-GHz electro-optic intensity modulator driven by an electronic pulsed waveform generated by the same arbitrary waveform generator and then amplified by a 12.5-GHz electronic amplifier. Fig. 8(c) shows the optical temporal waveform at the output of the pinhole, corresponding to a rectangular-like temporal pinhole with an intensity FWHM of ∼146 ps. Notice that this value is near the optimal one for the temporal imaging process demonstrated here below.

The results shown in Fig. 8 prove that the system implements the anticipated *time-to-frequency mapping* process, as demonstrated through the comparison between the signal optical spectrum [see Fig. 8(e)], measured at the output of the temporal pinhole using an optical spectrum analyzer with a resolution of 0.02 nm, and the input temporal optical waveform. The mapping is achieved along the expected spectral field of view of 11.6 nm, corresponding to an input temporal field of view of 23 ns. The spectral resolution that is estimated from the measurements in Fig. 8(e) is ∼0.0495 nm [32], closely approaching the theoretical spectral resolution of ∼0.046 nm; this latest value is obtained by numerical simulation using the method outlined in Section II. After the temporal pinhole, the light is sent through the output dispersive line, which introduces a dispersion of −692 ps/nm, and it is subsequently detected by a 45-GHz photo-detector and measured by a 28-GHz real-time oscilloscope. As shown in Fig. 8(f), the averaged output intensity waveform is a *temporally compressed "image"* of the input intensity waveform, with the expected magnification factor of $M = 1/2.86$, along the 8-ns output temporal field of view. The output resolution estimated from these measurements is ∼51.25 ps, in excellent agreement with the theoretically expected output resolution of ∼51 ps. Therefore, an experimental TBP of ∼156 is realized. As predicted, time gating is inherently performed by the system around the reference time defined by the pinhole time location [$\tau = 0$, in the plots Fig. 8(d)–(f)]. Fig. 8(g) shows the temporal intensity profile of the output image without averaging.

Fig. 9 illustrates the evolution of the signal along the experimentally demonstrated temporal compression system in Fig. 8. The numerically calculated carpet in Fig. 9 illustrates the evolution of the signal along the temporal compression system, including evolution through the input dispersion, temporal pinhole and output dispersion. Note that a carpet for coherent-light temporal pinhole-based imaging was shown in Ref. [4]; here we illustrate the carpet for an incoherent-light temporal compression system with the specifications and input signal of the experimental case reported above (results in Fig. 8). As a result of the limited system temporal field of view (23 ns at the input,

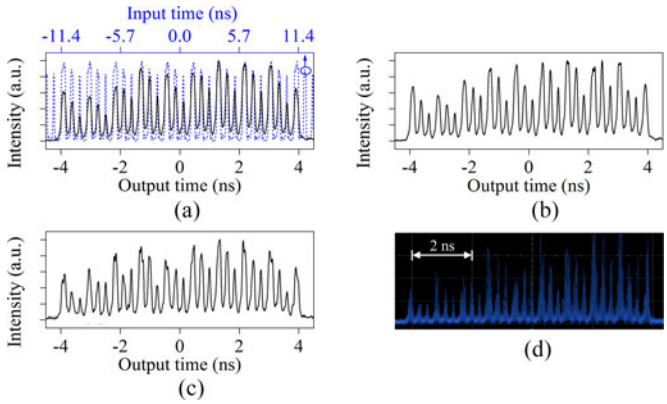

Fig. 10. Experimental demonstration of output images averaged over different times. (a) Input original waveform (dashed blue) and (a)–(c) corresponding output images (solid black) average for (a) 256, (b) 64, (c) 16 times. (d) The temporal intensity profile of the output image without averaging.

or 8 ns at the output), only nine consecutive periods of the original periodic temporal waveform are inherently selected at the pinhole location and subsequently imaged at the system output. All profiles along the process are averaged for 256 times.

Fig. 10 shows the quality of the output images in the described temporal compression experiment when averaged over different times. The input waveform [dashed blue in Fig. 10(a)] is averaged for 256 times. The corresponding output images (solid black) in Fig. 10(a)–(c) are averaged for 256, 64 and 16 times, respectively. In the representation in Fig. 10(a), the output and input time axes are relatively scaled according to the predicted magnification factor $M = 1/2.86$. Fig. 10(d) shows the temporal intensity profile of the output image without averaging. As shown in Fig. 10, there is an excellent agreement between the original waveform and output images. As expected, the quality of the output image is improved by use of a larger averaging. However, the input information can be still observed even with a very small number of averages or no averaging, e.g., as shown in Fig. 10(c) and (d).

B. Incoherent-Light Time-to-Frequency Mapping

The capability of the proposed scheme for implementing time-to-frequency mapping of incoherent-light intensity waveforms has been demonstrated in the example described above, Fig. 8(e). Fig. 11 shows additional experimental results on a system that has been specifically optimized for incoherent-light time-to-frequency mapping, offering a significantly improved TBP. In particular, a *Gaussian-like* temporal pinhole, instead of the *rectangular* temporal pinhole previously used in Section III-A, is now implemented in this experiment. The experimental setup is identical to that shown in Fig. 8, but here the input dispersion is -1326 ps/nm, the temporal pinhole has a Gaussian-like profile with an intensity FWHM of 95 ps [see Fig. 11(b)], and the incoherent-light source has a significantly larger spectrum, as shown in Fig. 11(a). The input signal (dotted blue) is a periodic three-pulse sequence (1110) of Gaussian-like pulses, which is shown in Fig. 11(e) (dotted blue curve). The intensity FWHM of the pulses in the input sequence is 95 ps and the inter-pulse time separation is 333 ps. The output spectrum is a mapped replica

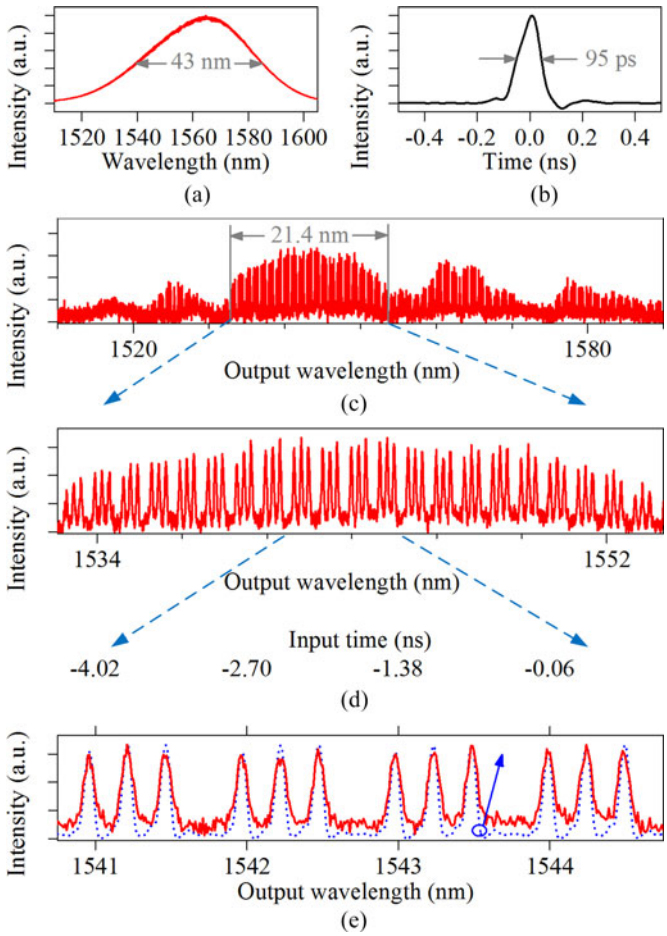

Fig. 11. Experimental demonstration of incoherent-light time-to-frequency mapping with improved TBP. (a) Gaussian-shaped spectrum of the incoherent light source. (b) Intensity profile of the Gaussian-like temporal pinhole. (c) Measured spectrum at the system output. (d) A close view of the output spectrum within the spectral field of view. (e) A still closer view of the output spectrum (solid red) compared with the scaled original temporal waveform (dotted blue), in which the scaling is fixed to be equal to the theoretical time-to-frequency mapping factor, i.e., 1326 ps/nm. In (a)–(e), profiles of the shown temporal waveforms are averaged for 256 times, whereas profiles of the spectra are averaged for ten times.

of the input signal but over a limited non-uniform spectral envelope, as shown in Fig. 11(c). The observed irregular spectral envelope is induced by the non-uniform shape of the incoherent light source spectrum combined with the strong polarization sensitivity of the electro-optic intensity modulator. A precise image of the input temporal waveform is achieved over a spectral field of view of $\sim$21.4 nm, corresponding to an input temporal field of view of $\sim$28.38 ns. Fig. 11(d) shows a closer view of the output spectrum within this spectral field of view. Fig. 11(e) shows a still closer view of the output spectrum (solid red) compared with the scaled original temporal waveform (dotted blue), in which the scaling is fixed to be equal to the theoretical time-to-frequency mapping factor, i.e., 1326 ps/nm. The output spectral resolution that is estimated from the measured data is $\sim$0.075 nm, corresponding to an input temporal resolution of 99.45 ps, closely approaching the theoretical output spectral and input temporal resolutions of $\sim$0.08 nm and $\sim$107.1 ps, respectively. Therefore, an experimental TBP of $\sim$285 is achieved.

IV. Discussions and Conclusion

A central conclusion of our work is that the temporal pinhole concept provides the key for the realization of time-domain equivalents of well-known spatial-domain signal-processing platforms on incoherent-light waveforms. The temporal imaging systems studied here should be particularly useful for generation, measurement, and processing of broadband RF waveforms, avoiding the need for ultrashort pulse laser sources, as required in previous schemes [7], [13], [15], [19].

A shortcoming of the incoherent methods is that the output waveform exhibits a poor signal-to-noise ratio, such that averaging over multiple realizations of the incoherent process is needed. This requirement limits the use of these techniques to temporally periodic waveforms and precludes their use on a single-shot basis. However, we anticipate that the system could be potentially upgraded for single-shot temporal imaging by replacing the incoherent continuous-spectrum light source with a suitable discrete-spectrum (multi-wavelength) laser source, a strategy that has been successfully demonstrated for other incoherent lightwave temporal signal-processing operations [38].

A related drawback of pinhole-based temporal imaging processes concerns their inherent low energy efficiency, imposed by the fact that the temporal pinhole filters out all the incoming signal energy outside the pinhole duration. Notice that improving the system time/frequency resolution typically requires using a shorter temporal pinhole, which in turn translates into a reduced energy efficiency. This may represent a critical drawback for practical uses of the pinhole-based temporal imaging methods. Solutions to this problem have been pursued in the spatial domain, e.g., using a multi-pinhole technique [39], and could also be potentially transferred for application on the temporal imaging problem. For instance, we have recently shown significant energy-efficiency improvements by using temporal modulation with a pinspeck (notch in an otherwise uniform modulation background) rather than a pinhole [40].

To conclude, this paper has presented a comprehensive theoretical analysis of a set of recently demonstrated schemes for incoherent-light temporal imaging based on the concept of a temporal pinhole. Analyzed systems include temporal magnification and compression, time-to-frequency mapping and frequency-to-time mapping processes, all involving a suitable combination of optical dispersive lines and a short temporal gate (pinhole). We have derived the main system performance specifications, including mapping factors and precise estimates of time/frequency resolutions and operation windows (field of view), as a function of design parameters, namely dispersion values and pinhole duration. Design equations for system performance optimization have been also obtained and tradeoffs have been pointed out and discussed. Our theoretical findings have been confirmed through numerical simulations and experiments. The work reported here provides a deeper insight into pinhole-based temporal imaging systems for incoherent-light signal processing and should be very useful for the design and optimization of these systems aimed at specific applications.

Appendix

In the analysis of pinhole-based incoherent-light temporal imaging systems in Section II, we used two types of approximations, respectively referred to as the short-pinhole approximation and the long-pinhole approximation. Under these two approximations, the impulse response functions of the analyzed systems, Eqs. (7), (23) and (38), can be greatly simplified, and as such, the systems' performance, e.g., resolutions, can be analyzed in an easier fashion.

Since the formats of Eqs. (7), (23) and (38) are similar, involving convolution of the scaled output image with the squared magnitude of a Fresnel integral, we build up here a generic equation and provide a detailed mathematical analysis of this equation, with a focus on the result of applying the two mentioned approximations. By replacing the generic variables and functions in the generic equation with the particular variables and functions in Eqs. (7), (23) and (38) the results of the analysis of these equations given in Section II can be directly obtained. The generic equation is given by

$$\langle G(x)\rangle \propto U(mx) \otimes \left| P(nx) \otimes h_G(nx) \right|^2, \qquad (50)$$

where $h_G(x) = h_{G0}\exp[jx^2/(2\ddot{\Phi}_G)]$ is the impulse-response function of a generic linear dispersive medium and $\ddot{\Phi}_G$ is the associated generic dispersion factor. Note that the following variable changes need to be carried out to obtain the equations in Section II: for incoherent-light time-to-frequency mapping (see Section II-A), $x = \omega$, $G(x) = \tilde{I}_{\mathrm{Out}}(\omega)$, $U(x) = I_{\mathrm{In}}(\omega)$, $m = -\ddot{\Phi}_{\mathrm{ID}}, n = \ddot{\Phi}_{\mathrm{ID}}$, and $\ddot{\Phi}_G = \ddot{\Phi}_{\mathrm{ID}}$; for incoherent-light temporal imaging (see Section II-B), $x = \tau$, $G(x) = I_{\mathrm{Out}}(\tau)$, $U(x) = I_{\mathrm{In}}(\tau), m = -\ddot{\Phi}_{\mathrm{ID}}/\ddot{\Phi}_{\mathrm{OD}}, n = \ddot{\Phi}_{\mathrm{Eff}}/\ddot{\Phi}_{\mathrm{OD}}$, and $\ddot{\Phi}_G = \ddot{\Phi}_{\mathrm{Eff}}$; and for incoherent-light frequency-to-time mapping (see Section II-C), $x = \tau, G(x) = I_{\mathrm{Out}}x(\tau), U(x) = \tilde{I}_{\mathrm{In}}(\tau), m = 1/\ddot{\Phi}, n = 1$, and $\ddot{\Phi}_G = \ddot{\Phi}$.

The squared magnitude of the term $P(nx) \otimes h_G(nx)$ can be interpreted as the system's impulse response in Eq. (50). As such, the convolution $P(nx) \otimes h_G(nx)$ will be the focus of our analysis here. Notice that this convolution term is essentially a *Fresnel integral*, modeling propagation of the scaled pinhole function *P*(*nx*) through the scaled generic linear dispersive medium defined above. To be more concrete, this Fresnel integral can be expressed as follows

$$P(nx) \otimes h_G(nx) = h_{G0}\exp\left(\frac{jn^2x^2}{2\ddot{\Phi}_G}\right)\int_{-\infty}^{\infty} P(\tau_1) \times \exp\left(\frac{j\tau_1^2}{2\ddot{\Phi}_G}\right)\exp\left(-\frac{jnx\tau_1}{\ddot{\Phi}_G}\right)d\tau_1. \qquad (51)$$

The short-pinhole approximation essentially involves the well-known far-field, or Fraunhofer, approximation of the Fresnel integral in Eq. (51). In particular, if the pinhole function $P(\tau_1)$ is confined to a time width shorter than $2\Delta\tau$, i.e., $|\tau_1| \le \Delta\tau$, so that

$$\left|\frac{1}{2\ddot{\Phi}_G}\Delta\tau^2\right| \ll \pi, \qquad (52)$$

then the phase factor $\exp[(j\tau_1^2)/(2\ddot{\Phi}_G)]$ within the integral in Eq. (51) is negligible, and Eq. (51) can be approximated by

$$\begin{aligned} P(nx)\otimes h_G(nx) \;\approx\; & h_{G0}\exp\left(\frac{jn^2x^2}{2\ddot{\Phi}_G}\right)\int_{-\infty}^{\infty}P(\tau_1) \\ & \times\exp\left(-\frac{jnx\tau_1}{\ddot{\Phi}_G}\right)d\tau_1 = \sqrt{2\pi}h_{G0} \\ & \times\exp\left(\frac{jn^2x^2}{2\ddot{\Phi}_G}\right)\tilde{P}\left(\frac{nx}{\ddot{\Phi}_G}\right). \end{aligned} \tag{53}$$

As expected, the result of the Fresnel integral in Eq. (51) is approximately proportional to the scaled Fourier transform of the pinhole function. Introducing the Fraunhofer approximation in Eq. (53) into Eq. (50), we obtain

$$\begin{aligned} \langle G(x)\rangle \;\propto\; & U(mx)\otimes\left|P(nx)\otimes h_G(nx)\right|^2 \\ \propto\; & U(mx)\otimes\left|\tilde{P}\left(\frac{nx}{\ddot{\Phi}_G}\right)\right|^2 \\ \propto\; & U(mx)\otimes\tilde{I}_{\mathrm{Pinhole}}\left(\frac{nx}{\ddot{\Phi}_G}\right). \end{aligned} \tag{54}$$

Concerning the long-pinhole approximation, this refers to the well-known Rayleigh range approximation of the Fresnel integral term $P(nx)\otimes h_G(nx)$, under which the pinhole undergoes a negligible distortion by the dispersive process. In particular, the Fresnel integral term can be expressed as a function of the corresponding functions in the Fourier domain as follows:

$$\begin{aligned} P(nx)\otimes h_G(nx) \;=\; & h_{G0}\exp\left(\frac{jn^2x^2}{2\ddot{\Phi}_G}\right)\int_{-\infty}^{\infty}P(\tau_1) \\ & \times\exp\left(\frac{j\tau_1^2}{2\ddot{\Phi}_G}\right)\exp\left(-\frac{jnx\tau_1}{\ddot{\Phi}_G}\right)d\tau_1 \\ =\; & h_{G0}\sqrt{\ddot{\Phi}_G}\exp\left(j\frac{\pi}{4}\right)\exp\left(\frac{jn^2x^2}{2\ddot{\Phi}_G}\right) \\ & \times\left\{\tilde{P}\left(\frac{nx}{\ddot{\Phi}_G}\right)\otimes\exp\left[-\frac{j\ddot{\Phi}_G}{2}\left(\frac{nx}{\ddot{\Phi}_G}\right)^2\right]\right\} \\ =\; & h_{G0}\sqrt{\ddot{\Phi}_G}\exp\left(j\frac{\pi}{4}\right)\int_{-\infty}^{\infty}\tilde{P}(\Omega) \\ & \times\exp\left(-\frac{j\ddot{\Phi}_G\Omega^2}{2}\right)\exp(j\Omega nx)\,d\Omega. \end{aligned} \tag{55}$$

For a pinhole that is sufficiently long, if the pinhole spectrum $\tilde{P}(\Omega)$ is confined to a bandwidth smaller than $2\Delta\Omega$, i.e., $|\Omega|\le\Delta\Omega$, so that

$$\left|-\frac{\ddot{\Phi}_G}{2}\Delta\Omega^2\right| \ll \pi, \tag{56}$$

then the phase factor $\exp[(-j\ddot{\Phi}_G\Omega^2)/2]$ within the integral in Eq. (55), is negligible and Eq. (55) can be approximated by

$$\begin{aligned} P(nx)\otimes h_G(nx) \;\approx\; & h_{G0}\sqrt{\ddot{\Phi}_G}exp\left(j\frac{\pi}{4}\right)\int_{-\infty}^{\infty}\tilde{P}(\Omega) \\ & \times\exp(j\Omega nx)\,d\Omega \\ =\; & h_{G0}\sqrt{\ddot{\Phi}_G}\exp\left(j\frac{\pi}{4}\right)P(nx). \end{aligned} \tag{57}$$

As expected, the Fresnel integral is approximately proportional to the input scaled pinhole function. Introducing the Rayleigh range approximation in Eq. (57) into Eq. (50), we obtain

$$\begin{aligned} \langle G(x)\rangle \;\propto\; & U(mx)\otimes\left|P(nx)\otimes h_G(nx)\right|^2 \\ \propto\; & U(mx)\otimes\left|P(nx)\right|^2 \\ \propto\; & U(mx)\otimes I_{\mathrm{Pinhole}}(nx). \end{aligned} \tag{58}$$

REFERENCES

[1] E. Treacy, "Optical pulse compression with diffraction gratings," *IEEE J. Quantum Electron.*, vol. 5, no. 9, pp. 454–458, Sep. 1969.

[2] B. H. Kolner and M. Nazarathy, "Temporal imaging with a time lens," *Opt. Lett.*, vol. 14, pp. 630–632, Jun. 1989.

[3] B. H. Kolner, "Space-time duality and the theory of temporal imaging," *IEEE J. Quantum Electron.*, vol. 30, no. 8, pp. 1951–1936, Aug. 1994.

[4] B. H. Kolner, "The pinhole time camera," *J. Opt. Soc. Am. A*, vol. 14, pp. 3349–3357, Dec. 1997.

[5] J. van Howe and C. Xu, "Ultrafast optical signal processing based upon space-time dualities," *J. Lightw. Technol.*, vol. 24, no. 7, pp. 2649–2662, Jul. 2006.

[6] R. Salem, M. A. Foster, and A. L. Gaeta, "Application of space-time duality to ultrahigh-speed optical signal processing," *Adv. Opt. Photon.*, vol. 5, pp. 274–317, Aug. 2013.

[7] W. J. Caputi, "Stretch: A time-transformation technique," *IEEE Trans. Aerosp. Electron. Syst.*, vol. AES-7, no. 2, pp. 269–278, Mar. 1971.

[8] A. W. Lohmann and D. Mendlovic, "Temporal filtering with time lenses," *Appl. Opt.*, vol. 31, pp. 6212–6219, Oct. 1992.

[9] A. W. Lohmann and D. Mendlovic, "Temporal perfect-shuffle optical processor," *Opt. Lett.*, vol. 17, pp. 822–824, Jun. 1, 1992.

[10] C. V. Bennett, R. P. Scott, and B. H. Kolner, "Temporal magnification and reversal of 100 Gb/s optical data with an up-conversion time microscope," *Appl. Phys. Lett.*, vol. 65, pp. 2513–2515, Nov. 1994.

[11] A. Bhushan, F. Coppinger, and B. Jalali, "Time-stretched analogue-to-digital conversion," *Electron. Lett.*, vol. 34, pp. 839–841, Apr. 1998.

[12] C. V. Bennett and B. H. Kolner, "Principles of parametric temporal imaging. I. System configurations," *IEEE J. Quantum Electron.*, vol. 36, no. 4, pp. 430–437, Apr. 2000.

[13] Y. Han and B. Jalali, "Photonic time-stretched analog-to-digital converter: Fundamental concepts and practical considerations," *J. Lightw. Technol.*, vol. 21, no. 12, pp. 3085–3103, Dec. 2003.

[14] J. Azaña, N. K. Berger, B. Levit, and B. Fischer, "Broadband arbitrary waveform generation based on microwave frequency upshifting in optical fibers," *J. Lightw. Technol.*, vol. 24, no. 7, pp. 2663–2675, Jul. 2006.

[15] J. Chou, O. Boyraz, D. Solli, and B. Jalali, "Femtosecond real-time single-shot digitizer," *Appl. Phys. Lett.*, vol. 91, 2007, Art. no. 161105.

[16] R. Salem, M. A. Foster, A. C. Turner, D. F. Geraghty, M. Lipson, and A. L. Gaeta, "Optical time lens based on four-wave mixing on a silicon chip," *Opt. Lett.*, vol. 33, pp. 1047–1049, May 2008.

[17] M. A. Foster, R. Salem, Y. Okawachi, A. C. Turner-Foster, M. Lipson, and A. L. Gaeta, "Ultrafast waveform compression using a time-domain telescope," *Nature Photon.*, vol. 3, pp. 581–585, Sep. 2009.

[18] M. Fridman, A. Farsi, Y. Okawachi, and A. L. Gaeta, "Demonstration of temporal cloaking," *Nature*, vol. 481, pp. 62–65, Jan. 2012.

[19] K. Goda and B. Jalali, "Dispersive Fourier transformation for fast continuous single-shot measurements," *Nature Photon.*, vol. 7, pp. 102–112, Jan. 2013.

[20] J. M. Lukens, D. E. Leaird, and A. M. Weiner, "A temporal cloak at telecommunication data rate," *Nature*, vol. 498, pp. 205–208, Jun. 2013.

[21] M. A. Foster, R. Salem, D. F. Geraghty, A. C. Turner-Foster, M. Lipson, and A. L. Gaeta, "Silicon-chip-based ultrafast optical oscilloscope," *Nature*, vol. 456, pp. 81–84, Nov. 2008.
[22] J. Azana and M. A. Muriel, "Real-time optical spectrum analysis based on the time-space duality in chirped fiber gratings," *IEEE J. Quantum Electron.*, vol. 36, no. 5, pp. 517–526, May 2000.
[23] J. van Howe, J. Hansryd, and C. Xu, "Multiwavelength pulse generator using time-lens compression," *Opt. Lett.*, vol. 29, pp. 1470–1472, Jul. 2004.
[24] D. J. Richardson, "Silicon photonics: Beating the electronics bottleneck," *Nature Photon.*, vol. 3, pp. 562–564, Oct. 2009.
[25] C. Dorrer, "Temporal van Cittert–Zernike theorem and its application to the measurement of chromatic dispersion," *J. Opt. Soc. Amer. B*, vol. 21, pp. 1417–1423, Aug. 2004.
[26] H. Lajunen, P. Vahimaa, and J. Tervo, "Theory of spatially and spectrally partially coherent pulses," *J. Opt. Soc. Amer. A*, vol. 22, pp. 1536–1545, Aug. 2005.
[27] V. Torres-Company, J. Lancis, and P. Andrés, "Incoherent frequency-to-time mapping: Application to incoherent pulse shaping," *J. Opt. Soc. Amer. A*, vol. 24, pp. 888–894, Mar. 2007.
[28] C. Dorrer, "Statistical analysis of incoherent pulse shaping," *Opt. Exp.*, vol. 17, pp. 3341–3352, Mar. 2009.
[29] Y. Park and J. Azaña, "Ultrahigh dispersion of broadband microwave signals by incoherent photonic processing," *Opt. Exp.*, vol. 18, pp. 14752–14761, Jul. 2010.
[30] H. Y. Jiang, L. S. Yan, Y. F. Sun, J. Ye, W. Pan, B. Luo, and X.-H. Zou, "Photonic arbitrary waveform generation based on crossed frequency to time mapping," *Opt. Exp.*, vol. 21, pp. 6488–6496, Mar. 2013.
[31] H. Lajunen, J. Turunen, P. Vahimaa, J. Tervo, and F. Wyrowski, "Spectrally partially coherent pulse trains in dispersive media," *Opt. Commun.*, vol. 255, pp. 12–22, Nov. 2005.
[32] B. Li and J. Azaña, "Incoherent-light temporal stretching of high-speed intensity waveforms," *Opt. Lett.*, vol. 39, pp. 4243–4246, Jul. 2014.
[33] H. Chen, C. Lei, F. Xing, Z. Weng, M. Chen, S. Yang, and S. Xie, "Multiwavelength time-stretch imaging system," *Opt. Lett.*, vol. 39, pp. 2202–2205, Apr. 1, 2014.
[34] C. Zhang, Y. Xu, X. Wei, K. K. Tsia, and K. K. Y. Wong, "Time-stretch microscopy based on time-wavelength sequence reconstruction from wideband incoherent source," *Appl. Phys. Lett.*, vol. 105, Jul. 28, 2014, Art. no. 041113.
[35] B. E. Saleh and M. C. Teich, *Fundamentals of Photonics*. New York, NY, USA: Wiley, 1991 ch. 10.
[36] P. Naulleau and E. Leith, "Stretch, time lenses, and incoherent time imaging," *Appl. Opt.*, vol. 34, pp. 4119–4128, Jul. 1995.
[37] W. C. Black, Jr., and D. Hodges, "Time interleaved converter arrays," *IEEE J. Solid-State circuits*, vol. 15, no. 6, pp. 1022–1029, Dec. 1980.
[38] A. Malacarne, R. Ashrafi, M. Li, S. LaRochelle, J. Yao, and J. Azaña, "Single-shot photonic time-intensity integration based on a time-spectrum convolution system," *Opt. Lett.*, vol. 37, pp. 1355–1357, Jan. 2012.
[39] G. Groh, G. S. Hayat, and G. W. Stroke, "X-Ray and γ-Ray imaging with multiple-pinhole cameras using a posteriori image synthesis," *Appl. Opt.*, vol. 11, pp. 931–933, Apr. 1972.
[40] B. Li, S. Lou, and J. Azaña, "Incoherent-light temporal imaging based on a temporal pinspeck," *IEEE Photon. Technol. Lett.*, vol. 27, no. 4, pp. 348–351, Feb. 2015.

Bo Li received the Ph.D. degree in telecommunication from Beijing Jiaotong University, Beijing, China, in 2015.

Under an exchange program from 2012 to 2014, he was with the Ultrafast Optical Processing Group at the Institut National de la Recherche Scientifique—Energie, Matériaux et Télécommunications—Université du Québec, Montréal, QC, Canada, under the supervision of Prof. J. Azaña. He is currently a Postdoctoral Researcher in Xu Group, Cornell University, Ithaca, NY, USA, under the supervision of Prof. C. Xu. His recent research interests include ultrafast optical signal processing, microwave photonics, multiphoton microscopy, and coherent anti-Stokes Raman scattering microscopy.

José Azaña received the Engineer degree and the Ph.D. degree in telecommunication engineering from the Universidad Politécnica de Madrid, Madrid, Spain. He is currently a Professor and a Canada Research Chair at the Institut National de la Recherche Scientifique, Centre Energie, Matériaux et Télécommunications, Montreal, QC, Canada. His research interests include ultrafast photonics, optical signal processing, all-fiber and integrated-waveguide technologies, high-speed telecommunications, all-optical computing, measurement of ultrafast events, light pulse interferometry, and broadband microwave signal generation and manipulation. He has to his credit nearly 400 publications in top scientific journals and technical conferences, including more than 160 contributions in high-impact peer-review journals (with most publications in the IEEE, OSA, and Nature editorial groups), and many invited and coinvited journal publications and presentations in leading international meetings.

His research work has been recognized with several prestigious awards and distinctions at institutional, national, and international levels, including the 2008 IEEE-Photonics Society Young Investigator Award, and the 2009 IEEE-MTT Society Microwave Prize.